Fuel 379 (2025) 132850

Contents lists available at ScienceDirect

Fuel

journal homepage: www.elsevier.com/locate/fuel

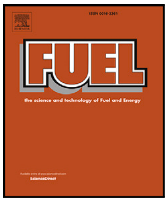

Full length article

Influence of aluminum nanoparticles in alternative fuel: Single droplet combustion experiments and modeling

Inês A.S. Ferrão [a,b,c], Tomás S.M. Mendes [b,c], Miguel A.A. Mendes [b], Ana. S.O.H. Moita [c], André R.R. Silva [a,*]

[a] *AEROG, Universidade da Beira Interior, Covilhã, Portugal*
[b] *IDMEC, Instituto Superior Técnico, Lisboa, Portugal*
[c] *IN+, Instituto Superior Técnico, Lisboa, Portugal*

ARTICLE INFO

Keywords:
Nanofuel
Single droplet
Radiation absorption
Biofuel

ABSTRACT

In this work, the effect of adding aluminum nanoparticles on hydrotreated vegetable oil was investigated experimentally and numerically in terms of nanofuel stability and single droplet combustion. The purpose is to understand the phenomena related to isolated droplet combustion when metallic particles are added to a liquid biofuel. Falling droplet combustion experiments were conducted in a drop tube furnace at two different furnace temperatures (800 °C and 1000 °C) using a high-speed camera coupled with a high magnification lens to investigate the droplet size evolution as disruptive burning phenomena. In numerical terms, a simplified macroscopic model was developed to predict the burning behavior of isolated nanofuel droplets, considering hexadecane as a surrogate fuel for the biofuel. The results reveal that adding nanoparticles resulted in a departure from the D^2-law. Moreover, an increase in the overall droplet burning rate was observed, and according to the numerical results, nanoparticle radiation absorption is the responsible mechanism. Micro-explosions occurred for all nanofuels, and this disruptive burning behavior substantially influenced the droplet lifetime.

1. Introduction

Unquestionably, air transportation has experienced continuous and pronounced growth year after year. Aviation is the second largest sector in transportation and operates mainly on jet fuel. This exclusive reliance on fossil fuels makes the aviation sector responsible for about 2% of global CO_2 emissions [1]. The continuous growth of this sector, alongside the environmental issues and the depletion of fossil fuels, has promoted the search for alternative, reliable, and sustainable energy sources that could supply the current fleet. From the different solutions that emerged, biofuels are considered the most promising technology in the short term [2]. Compared to other approaches, their implementation would require fewer aircraft structure and airport infrastructure changes and, therefore, less costs and investments [3].

Biofuels or alternative fuels are renewable energy sources derived from sustainable feedstock. They promote cleaner combustion and are potentially carbon neutral, as most of the amount of CO_2 released during their burning has been previously captured by the plants from which biofuels originated while these were growing. In this way, implementing biofuels can assume a significant role in the present global context. However, some drawbacks exist regarding low energy content, high viscosity, lower volatility properties, and high production costs [4,5]. In order to improve the combustion performance of biofuels, several studies have been centered on dispersing energetic or inert nanoparticles, i.e., particles in size between 1 nm and 100 nm, stably suspended in conventional liquid fuels. This new class of fuels is referred to as nanofluid fuels or nanofuels. Research has shown that the addition of metallic nanoparticles to liquid fuels brings several advantages, such as the increase of volumetric energy density, the enhancement of the catalytic activity, lower ignition delay, higher ignition probability, higher volumetric heat release rates, faster burning rates, among others [4,6]. However, nanofuels may have some inconveniences regarding long-term stability, emissions from the combustion of solid particles, combustion residues attaching to the walls of engines, or even damage. These disadvantages require a more profound comprehension in order to drive their application successfully. Moreover, the evaporation and/or combustion behavior of nanofuels are not fully understood, and further discussion is recommended. According to the literature, when nanoparticles are added to liquid fuel, the most reported outcome was that the evaporation/combustion process of nanofuel droplets does not

---

[*] Corresponding author.
E-mail address: andre@ubi.pt (A.R.R. Silva).

https://doi.org/10.1016/j.fuel.2024.132850
Received 27 May 2024; Received in revised form 2 August 2024; Accepted 17 August 2024

Nomenclature

$\dot{m}$	Mass flow rate (kg s^{-1}).
$\mathcal{D}$	Mass diffusivity coefficient (m^2/s).
A	Area (m^2).
a	Inner shell radius (m).
Al	Aluminum.
b	Outer shell radius (m).
$B_{o,q}$	Spalding heat transfer number.
c_p	Specific heat (J kg^{-1}K^{-1}).
$CNTs$	Carbon nanotubes.
D	Diameter (m).
DTF	Drop tube furnace.
G	Irradiation (W m^{-2}).
g	Acceleration due to gravity (9.81 m s^{-2}).
h_{fg}	Latent heat of vaporization (J kg^{-1}).
J	Radiosity (W m^{-2}).
k	Thermal conductivity (W m^{-1} K^{-1}).
k_B	Boltzmann constant ($1.38 \cdot 10^{-23}$ J K^{-1}).
K_c	Burning rate constant (m^2 s^{-1}).
L	Principal radius of the liquid meniscus (m).
m	Mass (kg).
P	Pressure (Pa).
q	Specific heat (J kg^{-1}).
r	Radius (m), radial coordinate (m).
T	Temperature (K).
t	Time (s).
U	Velocity (m s^{-1}).
X	Mass fraction.
Y	Volume fraction.

Greek Symbols

α	Absorptivity, half-filling angle (rad).
β	Coefficient of thermal expansion (K^{-1}).
Δr	Thickness of the radial shell (m).
Δt	Time interval (s).
γ_{lv}	Surface tension (N m^{-1}).
μ	Dynamic viscosity (Pa s).
ν	Kinematic viscosity (m^2 s^{-1}).
ρ	Density (kg m^{-3}), principal radius of the liquid meniscus (m).
σ	Stefan–Boltzmann constant ($5.67 \cdot 10^{-8}$ W m^{-2} K^{-4}), mechanical stress (Pa).
θ	Contact angle (rad).
ε	Shell porosity.
ε_d	Emissivity.

Subscripts

0	Initial condition.
1	Gaseous region inside the flame front.
2	Gaseous region outside the flame front.
ψ	Tangential direction.
amb, ∞	Ambient, air.
$boil$	Boiling point.
d	Droplet.
eff	Effective.
ext	External.
F	Fuel.
f	Flame.
g	Gas.
h	Half-filling angle.
inj	Injection.
int	Internal.
l, liq	Liquid.
m	Principal radius of the liquid meniscus.
Ox	Oxidizer.
r	Radial direction.
rad	Radiation.
s	Shell.

Acronyms and Abbreviations

Al	Aluminum.
$CNTs$	Carbon nanotubes.
$MWCNTs$	Multiwalled carbon nanotubes.

follow the classical D^2-law [7–10]. Fig. 1 illustrates the typical evaporative/burning behavior of an isolated nanofuel droplet compared to that of a conventional liquid fuel droplet.

After an initial heating phase, it has been observed that the evaporation or burning rate of nanofuel droplets is not approximately constant, but instead, it gradually decreases [8]. Several authors [4,11,12] have observed different phases during the droplet lifetime: (i) a heating phase; (ii) a steady-state phase, conventionally identified on the evaporation/combustion of liquid fuels; (iii) a dry-out phase, where the droplet diameter decline rate is significantly reduced; and (iv) disruptive behavior phase, where phenomena such as puffing and micro-explosions occur. Under certain conditions, the micro-explosions can also involve particle combustion [4,13,14]. The presence of disruptive burning phenomena in nanofuels combustion has been highly reported, regardless of particle size and concentration, leading to the partial or total disintegration of the primary droplet [11,15–17]. The evaporation/combustion of nanofuels is a highly complex, multi-phase phenomenon in which several processes occur simultaneously [18]. The main mechanisms of adding nanoparticles to liquid fuels have already been identified but not clearly understood. Those are (a) radiation absorption by the nanoparticles and (b) particle accumulation at the droplet surface. The former provides an additional energy budget, accelerating the heating [19–22] and enhancing the evaporation/burning rate [13,18,23,24] of the droplet, thus allowing a greater heat release rate. On the other hand, particle aggregation at the droplet surface creates a resistance to the evaporation of liquid fuel, suppressing the evaporation/burning rate [25,26]. Since these two mechanisms compete against each other to dominate the change in evaporation rate [27], some studies reported that the droplet evaporation/burning could be affected by particle concentration influencing the radiation absorption [4,24]. In this context, a question remains whether there is any optimal particle concentration that no longer enhances evaporation or burning rate by the radiation absorption. The increase in particle concentration also improves the particle accumulation rate at the droplet surface, reducing the evaporation/burning rate [18]. The study of higher nanoparticle concentrations can be related to the increase in the energy density of nanofuel. Conversely, the nanofuel stability is negatively affected. Accordingly, Ghamari and Ratner [13] found an optimum particle loading at which maximum droplet burning rate is achieved under their experimental conditions. Similar findings were supported by Yadav et al. [15] and Li et al. [28], indicating that a

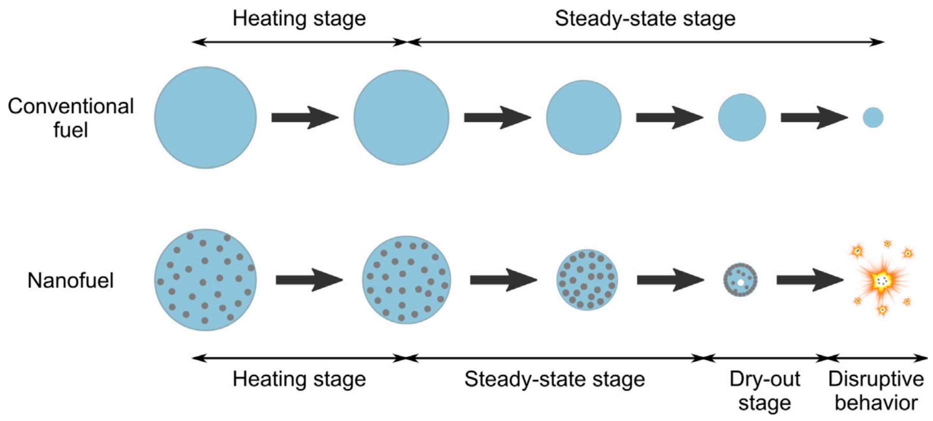

Fig. 1. Schematic of the typical nanofuel droplet dynamics compared to conventional fuel droplets.
Source: Adapted from [4,8].

burning rate enhancement can be achieved using nanoparticles until a specific concentration. Further increase of nanoparticle concentration in a droplet causes a higher agglomeration, negatively influencing the combustion process.

To better comprehend the behavior and dynamics of nanofuels, further experimental studies and the development of improved observational techniques are paramount to adapting these fuels to be viable for real-world applications. Visualizing and identifying the motion of nanoparticles within the droplet during evaporation and combustion processes will be explained in detail. However, cost, safety, time constraints, and challenging operating conditions can limit experimental studies. In this way, mathematical models can ease the phenomenological understanding of complex systems and predictions of the relevant processes. Consequently, developing numerical/analytical models capable of predicting the dynamics of liquid conventional fuels and nanofuels under different conditions is essential.

The classic combustion theory for isolated liquid fuel droplets was first proposed by Godsave [29] and Spalding [30] and is typically known as the D^2-law for droplet combustion. The model was developed based on an isolated, pure-component droplet burning in an oxidizing environment. Additionally, the convective effects can easily be included by using the film theory, as will be further discussed. The classic D^2-law, derived by assuming spherical symmetry, quasi-steadiness, and flame-sheet combustion, predicts the decrease of the square of the droplet diameter linearly with time. The model assumes constant average properties for the gas phase. While there can be significant variations in these properties from the droplet surface to the ambient surroundings, careful selection of mean values enables reasonably accurate predictions. To facilitate the comprehension, Table 1 displays the assumptions that yield a simplified model for single droplet combustion while preserving the essential physical processes.

The theoretical model focuses on predicting combustion characteristics, such as droplet size evolution and constant burning rate, based on the analytical solution for the fuel mass flow rate given by the following expression [31]:

$$\dot{m}_F = \frac{4\pi k_g r_s}{c_{pg}} \ln\left(1 + B_{o,q}\right) \tag{1}$$

where the Spalding heat transfer number, $B_{o,q}$, is defined as

$$B_{o,q} = \frac{\Delta h_c/\nu + c_{p,g}\left(T_\infty - T_s\right)}{h_{f,g}} \tag{2}$$

where Δh_c is the enthalpy of combustion, ν is the kinematic viscosity and $h_{f,g}$ is the latent heat of vaporization. It is assumed that the fuel droplet temperature is at its boiling point, $T_s = T_{boil}$ [32]. For very small droplets, the initial heating from ambient temperature up to boiling temperature happens rapidly and hence can be neglected.

Table 1
Assumptions made in the simplified model for single droplet combustion [31].

No.	Assumption
1	A spherical burning droplet, surrounded by a spherically symmetric flame is located in an infinite medium.
2	Combustion process is quasi-steady. This means that the process can be described as if it were in steady state at any instant in time.
3	Fuel is mono-component with zero solubility for gases, and phase equilibrium prevails at the liquid–vapor interface.
4	Pressure is constant and uniform.
5	The gaseous phase consists only of fuel vapor, oxidizer and combustion products.
6	Fuel and oxidizer react in stoichiometric proportions at the flame front. Chemical kinetics are assumed to be infinitely fast, resulting in an infinitesimally thin flame reaction sheet.
7	Lewis number, Le, defined as the ratio of thermal diffusivity to mass diffusivity, is unity.
8	Radiative heat transfer is negligible.
9	Liquid fuel is the only condensed phase, i.e., no soot or liquid water is present.

Consequently, the burning rate, K_c, is shown by the subsequent equation:

$$\frac{dD^2}{dt} = -K_c = \frac{8k_g}{\rho_l c_{p,g}} \ln\left(1 + B_{o,q}\right) \tag{3}$$

where k_g is the thermal conductivity of the gas, ρ_l is the liquid density and $c_{p,g}$ is the specific heat. The inclusion of the convective effects in D^2-law was previously reported by [31]. In this way, for a quiescent medium, $Nu_d = 2$, however, taking into account the convection effects, the burning rate can be defined as:

$$K_c = \frac{4k_g Nu_d}{\rho_l c_{pg}} \ln\left(1 + B_{o,q}\right). \tag{4}$$

Given that, the simplified basis of the D^2-law for droplet combustion represented in Eq. (5) states that the square of the droplet diameter decreases linearly with time as evaporation proceeds [32]. Considering the initial condition $D(t = 0) = D_0$, the D^2-law is represented by:

$$D^2 = D_0^2 - K_c t \tag{5}$$

The following sections will give a more detailed explanation of how this model can be applied to the current work. Over the years, an extensive investigation has been performed based on the classical evaporation and combustion model assumptions. In this context, numerous studies dedicated to the influence of ambient temperature, pressure, initial droplet diameter, convective effects on the droplet size evolution, and evaporation/combustion rate have been reported by the following authors [33–38]. The addition of nanoparticles to liquid fuel in numerical terms was also evaluated. Gan and Qiao [8] investigated the evaporation characteristics of liquid fuel with suspended aluminum nanoparticles under natural and weak forced convections at different temperatures. The population balance equation modeled the agglomeration process. Under certain conditions, a departure from the D^2-law was observed, and the nanofuels droplet evaporation rate gradually decreased. Results from a model based on the population balance equation suggest that particle agglomeration may cause the D^2-law deviation. The same authors [39] later studied the evaporation characteristics of nanofluid fuels experimentally with carbon-based nanostructures under radiation absorption in the ultraviolet–visible range. Furthermore, the optical properties were modeled using Rayleigh approximation. The results show that MWCNTs are more effective than Al and CNPs for radiation absorption in nanofluids because less energy is scattered away. More recently, Wei et al. [26] developed a model to predict the behavior of nanofluid droplets for the stage prior to particle shell formation and the deviation from the D^2-law. To date, only a relatively small number of models have been developed that explain the phenomena occurring during the evaporation/combustion of nanofuel droplets. The inclusion of particles in a liquid fuel affects the optical properties, which influences the nanoparticles absorption as well as the combustion process, as the particles will be retained within the droplet. Consequently, the burning rate is affected by these mechanisms that should be explored to understand the influence of adding nanoparticles in single droplet combustion.

In this context, the present study combines experimental and numerical investigation on nanofuel droplet combustion. Aluminum nanoparticles of 40 nm were added to the liquid sustainable aviation fuel. Firstly, a nanofuel stability study was performed to allow an investigation dedicated to a relatively high particle concentration (1.0, 2.0, and 4.0 wt.%). To accomplish it, nanofuels were prepared using a two-step method with chemical and physical processes. Subsequently, falling single droplet combustion experiments were carried out in a drop tube furnace (DTF) at two different furnace temperatures (T_∞ = 800 °C and T_∞ = 1000 °C). Visualization, combustion characteristics, and disruptive burning phenomena will be discussed. In terms of numerical analysis, a simplified theoretical model was developed to predict the burning behavior of isolated nanofuel droplets. The model estimates the droplet size evolution and burning rate, integrating several factors such as convective effects, radiation absorption, and particle agglomeration. This comprehensive approach enhances the understanding of these influences on the fuel, providing valuable insights for practical applications.

2. Materials and methods

2.1. Materials

Aluminum nanoparticles were chosen as an additive to the alternative liquid fuel. From the suitable candidates for hydrocarbon additives, aluminum was selected because of its energy content, abundance, and relatively low production costs [4]. As claimed by Starik et al. [40] and Wu et al. [41], aluminum is the most widespread metal on Earth, possesses a relatively large volumetric combustion enthalpy and is used as one component for solid propellants and high explosives to enhance heat release. Compared with micron-size particles, aluminum in the nanoscale present a lower melting point and better dispersion in liquids due to its size reduction.

Spherical aluminum nanoparticles, 99.995% pure, metal basis, indicating an average diameter of 40 nm, were purchased from Nanografi. Fig. 2 shows SEM (scanning electron microscopy) and TEM (transmission electron microscopy) images of aluminum nanoparticles confirming the spherical shape of the nanomaterial. The base fuel used was hydrotreated vegetable oil (HVO). This alternative fuel was acquired from Neste and is commonly referred to as renewable diesel with a commercial name of NExBTL. This biofuel is a mixture of straight chain and branched alkanes, with typical carbon numbers ranging from C_{15} to C_{18} [42], and features negligible amounts of sulfur and aromatics. Moreover, there was no noticeable oxidation of metal nanoparticles during the nanofuel production. All these materials were used as received without any additional treatment. A more detailed description, including the physical properties of HVO and aluminum, is presented in [4,14].

As previously mentioned, the present work focus on the combustion of nanofuel droplet with high particle concentration. Due to this, the nanofuel must remain stable during the droplet experiments regardless of the particle concentration. In order to ensure the stability of nanofuels and to allow the study of higher particle concentrations, a surfactant, oleic acid (OA) pure, pharma grade, procured from PanReac AppliChem ITW Reagents, was employed for the chemical stabilization of aluminum nanoparticles in HVO. Oleic acid was also tested in a few studies involving hydrocarbons and aluminum nanoparticles, and the results display that its addition improves the stability of the nanofuel [43–45]. However, besides its benefits in stability, adding surfactant in a nanofuel may affect the droplet combustion process resulting in higher complexity. The selection of surfactant was also based on its physical properties. Thus, the volatility of oleic acid closely matches that of the base fuel, which refers to the boiling point of OA (360 °C) and the final boiling point of HVO (308 °C). This feature is particularly significant when examining multi-component fuel systems.

2.2. Nanofuel preparation

In previous studies [4,14], the higher particle concentration tested by the authors was 1.0 wt.%. Particle concentrations >1.0 wt.% were impractical for single droplet experiments due to the lack of stability in nanofuel. Consequently, the present investigation introduces a surfactant in the nanofuel to enhance nanoparticle dispersion in the liquid biofuel.

Three nanofuels with aluminum nanoparticle concentrations of 1.0 wt.%, 2.0 wt.% and 4.0 wt.% were prepared and tested. In a theoretical approach, the increment of aluminum particle concentration increases the energy content of the fuel, a desired outcome for the mobility industry. Pure HVO and mixtures of HVO and OA were also tested for comparison purposes. The procedure for preparing liquid fuel mixtures of HVO and OA was straightforward. OA was first added to HVO on a weighing scale, and then the fuel blend was vigorously mixed for 10 min.

Regarding nanofuels preparation, a more precise and appropriate procedure needed to be executed. The purpose is to obtain stable suspensions with a low level of agglomeration for the experiments. Nanofuels were prepared through the two-step method. To obtain the desired particle concentration, aluminum nanoparticles were first added to HVO on a weighing scale. Subsequently, the HVO + Al was vigorously stirred for 20 min using a magnetic stirrer. The next step involved sonication. A probe sonicator UP200Ht (Hielscher) was used to suspend the nanoparticles and breakdown the agglomerates. The nanofuels were sonicated in an ice bath to maintain a constant temperature. Oleic acid was then added to the nanofuel and the mixture was, at last, vigorously stirred for an additional 10 min using a magnetic stirrer. The sonication time and amplitude, as well as the concentration of surfactant added, were optimized through a sedimentation analysis carried out by visual inspection, so that the longest stability possible was attempted. The fuel mixtures were sonicated for 30 min with an amplitude of 40%, and OA was added to the nanofuels in a surfactant-to-nanoparticle mass ratio of 1:1. Under these conditions, it was possible to obtain stable nanofuels for a period well beyond the approximately four hours of the experiments. However, to further

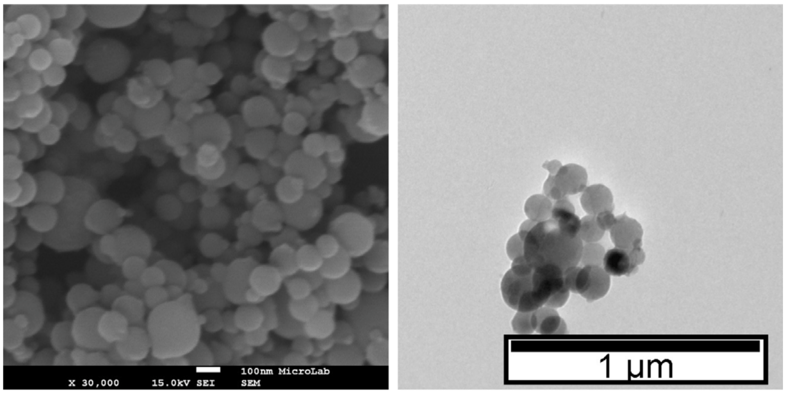

(a)

(b)

Fig. 2. Scanning electron microscopy (a) and transmission electron microscopy (b) images of aluminum nanoparticles.

implement nanofuels in real engines, an exhaustive study on stability should be performed in future works.

After the nanofuels preparation, their physical properties were measured. Fig. 3 shows the measurements of the variation in the density, surface tension, and viscosity as a result of the addition of nanoparticle and surfactant using a mass ratio of 1:1. The measurements are displayed in terms of (a), (c), (e) absolute values and (b), (d), (f) relative percentages to the HVO, respectively. The black, blue and red symbols correspond to the density, surface tension and viscosity measurements, respectively. The density was measured with a portable density/specific gravity meter DA-130N (Kyoto Electronics Manufacturing) and the viscosity with a viscosimeter DV3T (AMETEK Brookfield) with an accuracy of ±5%. The surface tension was determined by the pendant drop method using an optical tensiometer THETA (Attension). All measurements were performed at room temperature and atmospheric pressure. Results show that density and surface tension are not significantly influenced by the addition of particles and surfactant (<5 wt.%). On the contrary, the viscosity presents a considerable increase when nanoparticles and surfactant are added to HVO.

2.3. Experimental setup

Fig. 4 presents a schematic of the experimental setup dedicated to the single droplet experiments. It is composed of a drop tube furnace (DTF), a droplet generation apparatus, an illumination set, and an image acquisition system. The DTF contains electrical coils around a vertical quartz tube with an inner diameter of 6.6 cm and a length of 82.6 cm, in which droplet combustion occurs. It also has a water-cooled injector designed for liquid fuels placed at the top of the DTF. As previously mentioned, experiments were conducted at T_∞ = 800 °C and T_∞ = 1000 °C. To allow the visualization of single droplet combustion, the DTF has two opposed rectangular windows with 2 cm width and 20 cm height. Regarding the air supply, an air flow rate of 5.7 L/min with an accuracy of ±2% was employed in order to ensure a stable laminar air flow inside the DTF.

To generate droplets and inject them into the DTF, a monosize droplet generator MDG100 (TSI) was placed above the DTF injector inlet and aligned with its centerline. It is connected to a function generator PM5136 (Fluke) that can provide square waves with an amplitude of up to 20 Vpp and a frequency ranging from 0.1 MHz to 5 MHz. Fuel is fed into the MDG using 50 mL glass syringe coupled to a syringe pump NE-1000 (New Era Pump Systems). For the experiments, a pinhole with a diameter of 200 μm was attached to the MDG tip, a frequency of 2.07 kHz was supplied by the signal generator, and the syringe pump delivered a 1.32 mL/min flow rate. Under these conditions, droplets with an initial diameter of D_0 = 250 ± 12 μm were produced. A rotating disk with a slot was placed between the monosize generator and the entrance of the injector. The disk has a diameter of 12 cm, and the slot dimensions are 1 × 1 cm. It was inserted into an electric motor connected to a DC power supply of 2 A with an adjustable voltage between 3 to 12 V. In the experiments carried out, the voltage of the power supply was set at 3 V, imposing a rotational speed of 1200 rpm on the disk. Consequently, only the droplets that pass through the disk slot enter the DTF, being possible to ensure an inter droplet spacing of at least 50 droplet diameters. Therefore, no interaction between neighboring droplets occurs, and the phenomenon of single droplet combustion is guaranteed. An image of the present experimental setup is also presented in Appendix A.

Backlight imaging was chosen to study the phenomena occurring inside the DTF. This well-established technique involves aligning a light source with an image acquisition system and a test object, in this case, a fuel droplet. To ensure the complete acquisition of the droplet lifetime, the system was placed in approximately five different vertical positions along the DTF for each experiment. An LED light and a diffusing glass were placed in front of one of the DTF windows to increase the contrast. On the opposite side, an image acquisition system was correctly positioned in front of the other DTF window. It is composed of a high-speed camera CR600 × 2 (Optronis), a high magnification lens Zoom 6000® Lens System (Navitar) attached to the camera, and a computer that triggers the camera and stores the collected images for further analysis. During the experiments, a resolution of 1280 × 500 px, a frame rate of 1000 fps, and an exposure time of 1/12000 s were used. After each experiment, the system was calibrated using a reference with 76 μm diameter positioned in the focal plane to convert the scale from pixel to micron. The pixel-micron ratio obtained in the experiments ranged between 0.079 px/μm and 0.092 px/μm. Fig. 5 shows the temperature profiles inside the DTF. The temperature of the wall can reach up to 1200 °C, with this value being controlled by two type-S thermocouples. The temperature profiles along the center of the quartz tube, where droplets travel and burn, were measured for the wall temperature conditions in which the experiments in this study were carried out (T_∞ = 800 °C and T_∞ = 1000 °C). To perform such measurements, a type-R thermocouple with a diameter of 76 μm, inserted on an appropriate probe, was used. The probe was fixed on a linear motion mechanism, allowing for the thermocouple to move vertically along the center of the quartz tube with a precision of ±1 mm. Temperature values were taken from a data acquisition board connected to a computer, and the acquisition time at each position was such that the difference between the two readings was negligible. Near the injector tip (x = 0 cm), air temperature is lower than in regions further down. This is due to the interaction of the hot air with the water-cooled injector tip.

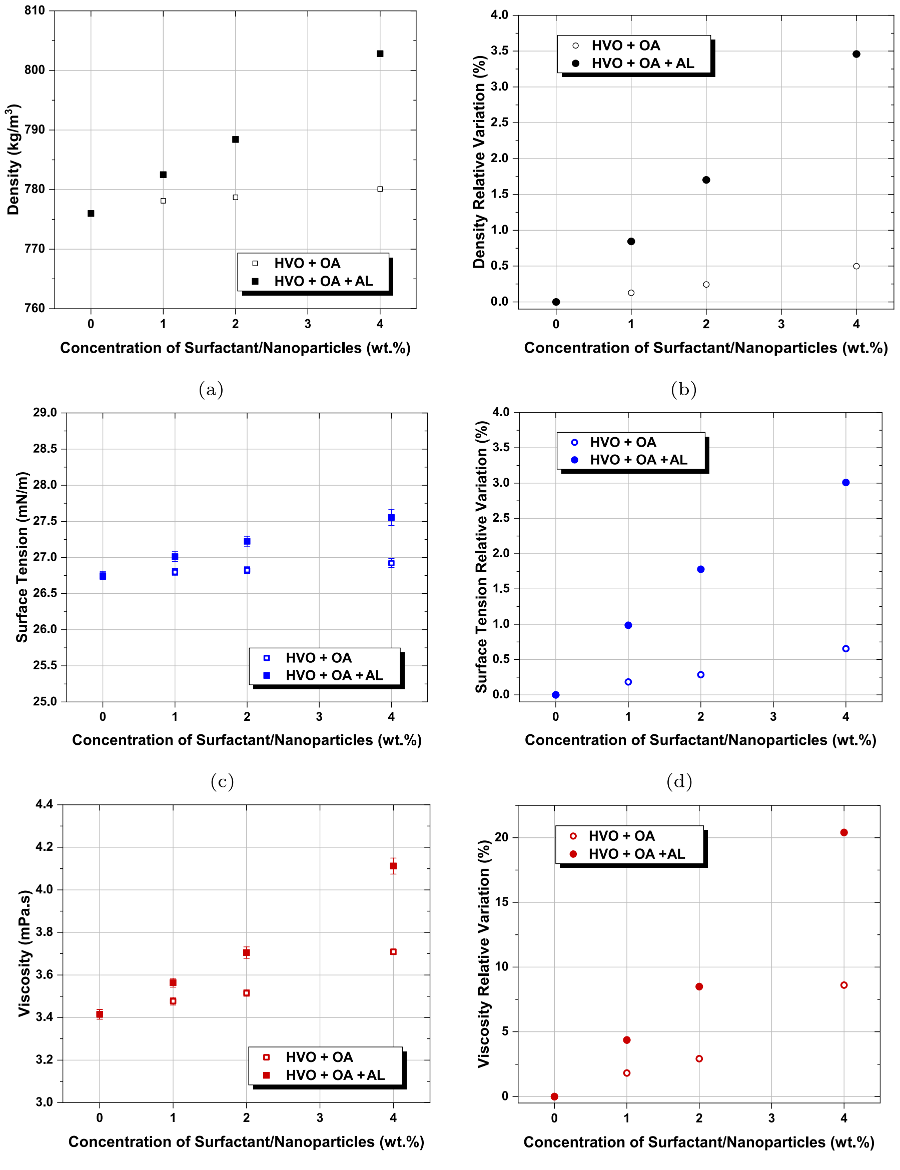

(a) (b) (c) (d) (e) (f)

Fig. 3. Physical properties measurements of density, surface tension and viscosity: (a), (c), (e) Absolute values; (b), (d), (f) relative variation to the HVO. (For interpretation of the references to color in this figure legend, the reader is referred to the web version of this article.)

Table 2
Airflow regime for experiments conditions.

	T_∞ = 800 °C	T_∞ = 1000 °C
Airflow velocity, U_∞ (m/s)	0.10	0.12
Kinematic viscosity of air, ν_{air} (m^2/s)	1.38 · 10^{-4}	1.82 · 10^{-4}
L (m)	0.066	0.066
Reynolds number, Re	48.85	43.69

The experimental study was first dedicated to the analysis of the operating conditions. The Reynolds number of the airflow was determined by the expression displayed in Eq. (13) and mean airflow velocity U_∞, by Eq. (37). Table 2 shows the Reynolds number inside the drop tube furnace at the two furnace temperatures.

The results show that a laminar airflow regime with reduced turbulence intensity is guaranteed inside the quartz tube. Consequently, the experimental setup provides a stable and suitable atmosphere for conducting single droplet experiments.

2.4. Image data processing

An image processing algorithm was developed to detect the droplets from the frames recorded and determine their characteristics, such as droplet diameter and droplet velocity. In this work, data was treated in ImageJ Software, an open-source software for analyzing and processing images. After each set of experiments, the recorded videos were reviewed and the frames in which focused droplets appeared were exported for further analysis. When analyzing each frame, a region of interest, including the droplet and its flame, was selected. Then, the threshold was adjusted for precise detection and measurement of the droplet. This study allowed the edge detection and pixel values through the Huang threshold method [46]. With the threshold correctly adjusted, the droplet projected area was obtained, from which the droplet diameter could be calculated. To determine the droplet velocity, the droplet centroid coordinates were measured for consecutive frames, and the distance between these points was determined, consequently divided by the frames time difference. Finally, these parameters were

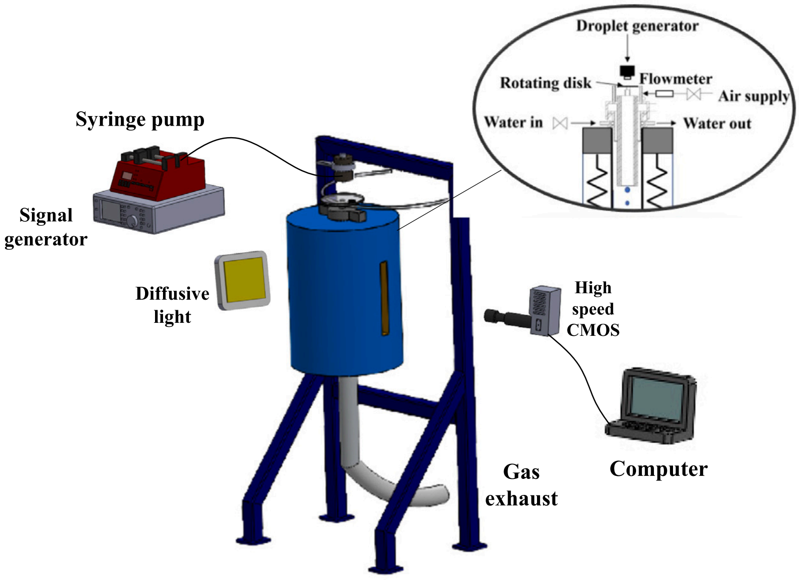

Fig. 4. Illustration of single droplet experimental setup.
Source: Adapted from [14].

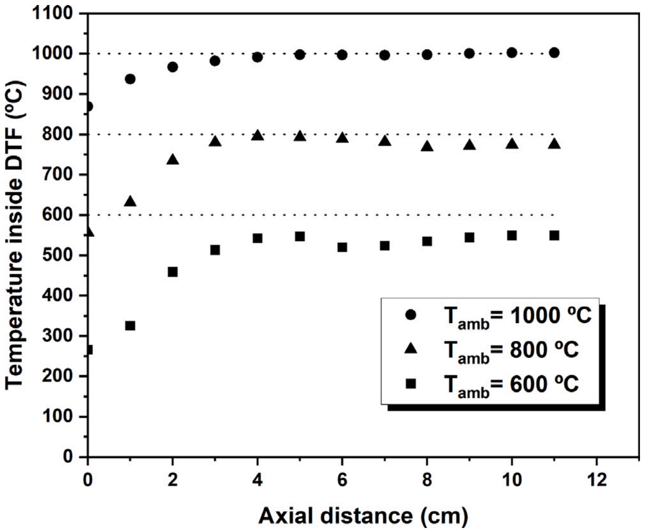

Fig. 5. Furnace temperature at the center of the DTF as a function of the axial distance for the respective wall temperature conditions (P_∞ = 1 atm), adapted from [14]. The injector tip is located at x = 0 cm.

stored to evaluate how they changed during combustion. A statistical study concluded that at least 35 droplets were needed to guarantee that the droplet size evolution curve and burning rate were independent of the sample size [4].

2.5. Mathematical model

As stated previously, the experimental data will be compared to the predictions generated by the mathematical model. To better understand the combustion phenomena associated with isolated nanofuel droplets, a simplified macroscopic model was developed using the Python programming language, as depicted in Fig. 6. A brief description of the mathematical model is provided in this section.

The basis of the mathematical model remains in the D^2 law. However, several assumptions will be adopted. Firstly, the thermophysical properties were simplified since HVO is a multi-component fuel. Due to the volatility and the thermophysical properties of such components not differing significantly, the burning behavior of HVO is expected to be approximately similar to a single-component fuel. It mainly comprises alkanes with typical carbon numbers from C_{15} to C_{18} [42]. Hexacadecane ($C_{16}H_{34}$) was tested as a surrogate fuel of HVO as well as HVO with OA, being one of the main constituents of biofuel. This specific approach was employed to simplify the modeling complexities. Consequently, hexadecane was selected, being one of the heaviest components in HVO [47]. Besides that, the effects of convection and the effects of the main mechanisms identified in the literature that arise from the addition of nanoparticles on liquid fuels were also included. These mechanisms are radiation absorption and particle agglomeration.

Considering the simplified interpretation of the D^2-law for droplet combustion, as indicated by Eq. (5), the thermophysical properties were evaluated following the approach of Law and Williams [48]. This approach allows accurate theoretical predictions against a large amount of experimental data over various conditions. Moreover, it is also assumed that the environment temperature is equal to the furnace temperature, T_∞. This assumption is reasonable as seen in Fig. 5. The authors [48] suggested calculating the liquid fuel density at the droplet surface temperature

$$\rho_l = \rho_l\left(T_s\right) \tag{6}$$

and proposed the following approximations for the gas thermal conductivity and the gas specific heat, respectively,

$$k_g = \overline{\chi} k_F\left(\overline{T}_1\right) + \left(1-\overline{\chi}\right) k_{Ox}\left(\overline{T}_1\right) \tag{7}$$

$$c_{pg} = c_{pF}\left(\overline{T}_1\right) \tag{8}$$

where k_F and k_{Ox} are the thermal conductivities of fuel vapor and oxidizer, the air in the present case, $\overline{\chi}$ is related to an average fuel mole fraction in the gaseous region inside the flame front (Appendix B). A value of 0.4 was considered since it provides a good agreement with experiments [48]; and c_{pF} is the specific heat of fuel vapor. The authors also proposed to evaluate the properties presented in Eqs. (7) and (8) at an average temperature of $\overline{T}_1 = \left(T_s + T_f\right)/2$, as previously

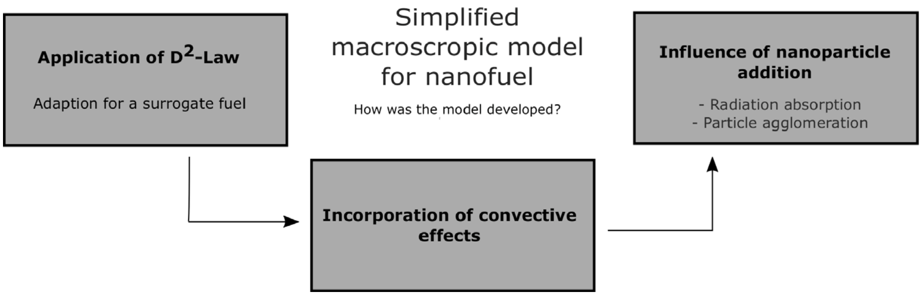

Fig. 6. Schematic diagram of the analytical approach of the simplified macroscopic model for nanofuel droplets.

mentioned the region inside the front flame. To estimate the flame temperature, denoted as T_f, based on the thermophysical properties, an assumption was considered that exhibits negligible deviation from the adiabatic flame temperature observed in a stoichiometric system under constant pressure. In this system, the initial fuel temperature corresponds to its boiling point, T_{boil}, while T_∞ represents the initial air temperature. Despite the potential for dissociation to decrease the flame temperature, particularly under stoichiometric conditions and high environment temperatures, incorporating its effect into the flame temperature estimation would introduce further complexity. Hence, disregarding the influence of the dissociation on the flame temperature was deemed appropriate to maintain simplicity.

In the present work, a falling single droplet combustion experiment is employed where the heat and mass transfer processes are influenced by external convection, which usually affects the droplet burning rate [49]. The Richardson number was estimated to determine the importance of natural convection relative to forced convection for the conditions under which the experiments were conducted.

$$Ri_d = \frac{Gr_d}{Re_d^2} \tag{9}$$

Generally, if $Ri_d \ll 1$, natural convection effects may be ignored. Conversely, forced convection effects may be neglected if $Ri_d \gg 1$. Otherwise, for $Ri_d \approx 1$, the combined effects of free and forced convection must be considered [50]. According to Law and Williams [48], the droplet Grashof number is defined as

$$Gr_d = \frac{g\beta_g\left(T_f - T_\infty\right)D^3}{\nu_g^2} \tag{10}$$

where g is the acceleration due to gravity, β_g is the gas coefficient of thermal expansion, $\beta_g \simeq 1/T_g$ for ideal gases and ν_g is the gas kinematic viscosity. The droplet Reynolds number can be written as follows [48]

$$Re_d = \frac{U_{rel}D}{\nu_g} \tag{11}$$

where D is the droplet diameter and U_{rel} is the relative velocity between the droplet and the free stream that can be determined by the following expression:

$$U_{rel} = U_d - U_\infty\,. \tag{12}$$

It is relevant to distinguish the droplet Reynolds number from the airflow Reynolds number. The former is expressed by

$$Re = \frac{U_\infty L}{\nu_{air}}\,. \tag{13}$$

In the above expression, L corresponds to the characteristic length represented in the present work as $D_{tube} = 0.066$ m. The kinematic viscosity of air is portrayed as ν_{air}.

Therefore, only forced convection is expected to influence the droplet burning rate, whereas natural convection can be neglected, as displayed in Table 3. Since the present work incorporates the convective effects, the burning rate can be defined in Eq. (4). A detailed description of the convective effects in the present mathematical model is presented in Appendix C.

Table 3
Estimated magnitude order from experimental results.

Parameters	Order of magnitude ($\mathcal{O}$)
g	$10\,\mathrm{m\,s^{-2}}$
β_g	$10^{-3}\,\mathrm{K^{-1}}$
$\left(T_f - T_\infty\right)$	$10^{3}\,\mathrm{K}$
D^3	$10^{-11}\,\mathrm{m^3}$
ν_g^2	$10^{-7}\,\mathrm{m^4\,s^{-2}}$
Gr_d	10^{-3}
U_{rel}	$1\,\mathrm{m\,s^{-1}}$
D	$10^{-4}\,\mathrm{m}$
ν_g	$10^{-4}\,\mathrm{m^2\,s^{-1}}$
Re_d	1
Ri_d	$10^{-3} \ll 1$

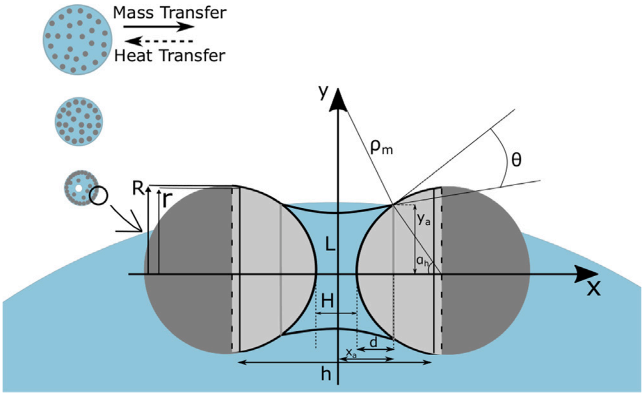

Fig. 7. Schematic of a liquid bridge between two particles.
Source: Adapted from [51].

2.6. *Incorporation of nanoparticles in a liquid droplet*

When nanoparticles are added to liquid fuel, two main mechanisms should be explored: radiation absorption and particle agglomeration. The influence of radiation is usually neglected, as reported in Table 1. Radiation absorbed by the droplet is frequently neglected since most liquid fuels are considered transparent to radiation [52]. In this respect, thermal conduction only accomplishes heat transfer to the droplet surface. According to the literature, the radiative heat transfer can become significant as the nanoparticles suspended in the droplet absorb the radiation energy emitted by the droplet flame and, in some cases, by an external heating source. Consequently, the radiation absorption

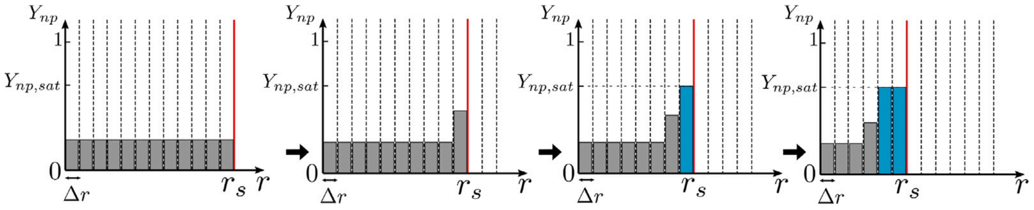

Fig. 8. Schematic of the numerical approach to obtain volume fraction profile of nanoparticles inside the droplet.

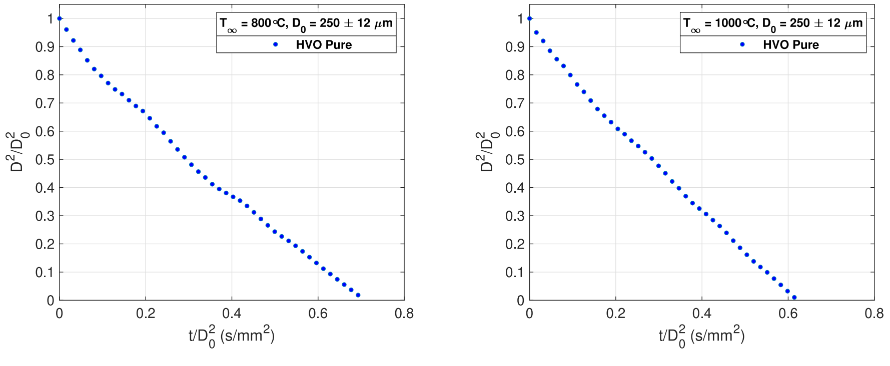

(a)

(b)

Fig. 9. Droplet size evolution of pure HVO for (a) $T_\infty = 800$ °C. (b) $T_\infty = 1000$ °C.

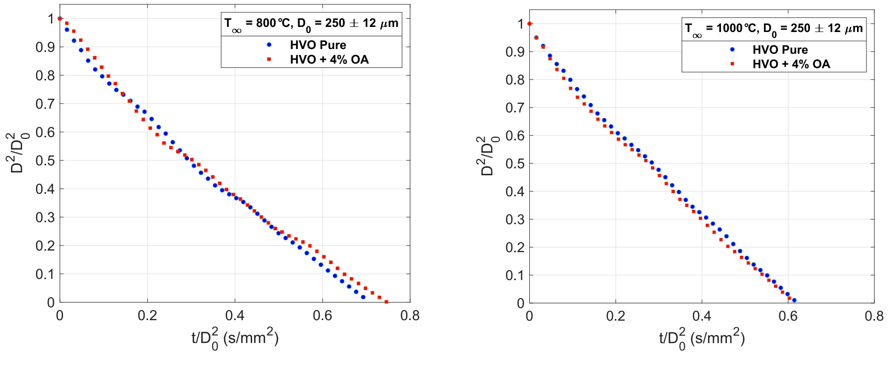

(a)

(b)

Fig. 10. Droplet size evolution of pure HVO and HVO with the addition of 4.0 wt.% of OA for: (a) $T_\infty = 800$ °C. (b) $T_\infty = 1000$ °C.

increases the energy per unit of time available to vaporize the droplet, affecting the burning rate of nanofuel droplets.

To include the effects of radiative heat transfer in the simplified macroscopic model resulting from the addition of nanoparticles, blackbody radiation was assumed to be emitted from infinity, i.e., from the DTF walls in a spherically symmetric field. The blackbody radiation assumption is due to the surface of the DTF walls being much larger than the droplet surface [53]. It was also considered that the gaseous phase surrounding the droplet is passive to radiation. This means that the interaction between the gas phase and the radiation is neglected. Furthermore, since droplets with an initial diameter of 250 ± 12 μm were studied and Marchese and Dryer [54] demonstrated that the radiative heat losses from droplet flames are only significant for droplet diameters greater than 1 mm, the radiative heat transfer from the flame was neglected. Based on this, the effect of the radiation absorption should be included in the surface energy balance at the droplet liquid–vapor interface. Consequently, the heat transferred into the droplet surface is now given by

$$-\left[-k_g 4\pi r^2 \frac{dT}{dr}\right]_{r_s} + \dot{Q}_{rad} = \dot{m}_F h_{fg} \tag{14}$$

where $\dot{Q}_{rad}$ is the net radiation heat transfer rate at the droplet surface, determined as follows

$$\dot{Q}_{rad} = A_d \left(G_w - J_d\right) = A_d \sigma \left(\alpha_d T_w^4 - \varepsilon_d T_s^4\right) \tag{15}$$

where A_d is the droplet surface area, G_w is the DTF walls irradiation, J_d is the droplet radiosity, σ is the Stefan–Boltzmann constant and α_d and ε_d are, respectively, the droplet absorptivity and emissivity.

The infrared spectrum was acquired by Fourier transform infrared spectroscopy (FTIR) using a Nicolet iS10 spectrometer (Thermo Scientific, Inc., MA, USA) at a range of v_{rad} = 4000 to 400 cm^{-1}. The wavenumber is expressed by

$$v_{rad} = \frac{1}{\lambda} \tag{16}$$

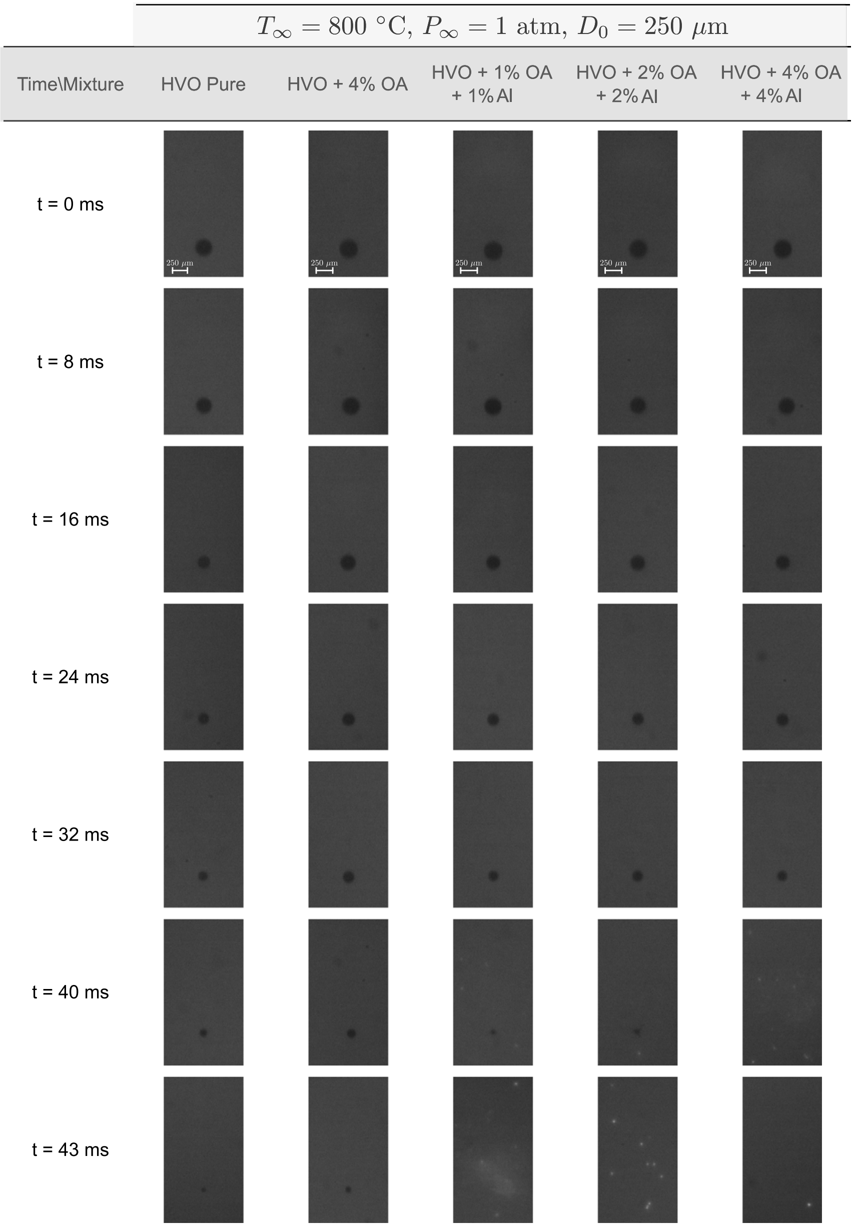

Fig. 11. Sequence of instantaneous images of the tested fuels at a furnace temperature of $T_\infty = 800$ °C.

The spectra were recorded using pure HVO as a background, highlighting the nanoparticles absorbance. Therefore, this approach will focus on the influence of particle concentration variation, evidencing the role of this parameter in nanofuel droplet combustion. Consequently, the volumetric absorptivity displayed in Eq. (17) is determined for each nanofuel with different particle concentrations given by the following equation [55,56]

$$\alpha = 1 - e^{-\alpha_\lambda \cdot D_m} \tag{17}$$

where α_λ is the absorption coefficient at different bands, $\lambda = 2.7$ μm and $\lambda = 4.3$ μm, which corresponds to the combustion products CO_2 and H_2O and $\lambda = 7.0$ μm. D_m is the mean beam length of a sphere represented by Eq. (18) adapted from [53].

$$D_m = 0.65D \tag{18}$$

The emissive power of DTF walls was determined by the equation [53]:

$$E(\lambda, T_\infty) = \frac{C_1}{\lambda^5\left[exp(C_2/\lambda T_\infty) - 1\right]} \tag{19}$$

where $C_1 = 3.7 \times 10^8$ W μm^4 m^{-2}, $C_2 = 1.4 \times 10^4$ μmK, T_∞ the tested furnace temperatures and λ considered in Eq. (16).

It is noteworthy that in the present work, the radiation energy from DTF walls is mainly absorbed by the nanoparticles. Subsequently, thermal conduction is employed to raise the temperature of the liquid fuel that covers the nanoparticles.

Defining, for convenience, $q_{rad} = \dot{Q}_{rad}/\dot{m}_F$ and substituting into Eq. (14), yields

$$-\left[-k_g 4\pi r^2 \frac{dT}{dr}\right]_{r_s} = \dot{m}_F\left(h_{fg} - q_{rad}\right) \tag{20}$$

which provides a revised definition of the effective latent heat of vaporization

$$h_{fg,eff} = h_{fg} - q_{rad}\,. \tag{21}$$

Thus, the droplet size evolution continues to be determined by Eq. (5), and K_c is still evaluated by Eq. (4). Thus, $B_{o,q}$ is calculated by Eq. (22) for nanofuel droplets emphasizing the primary outcome of the original

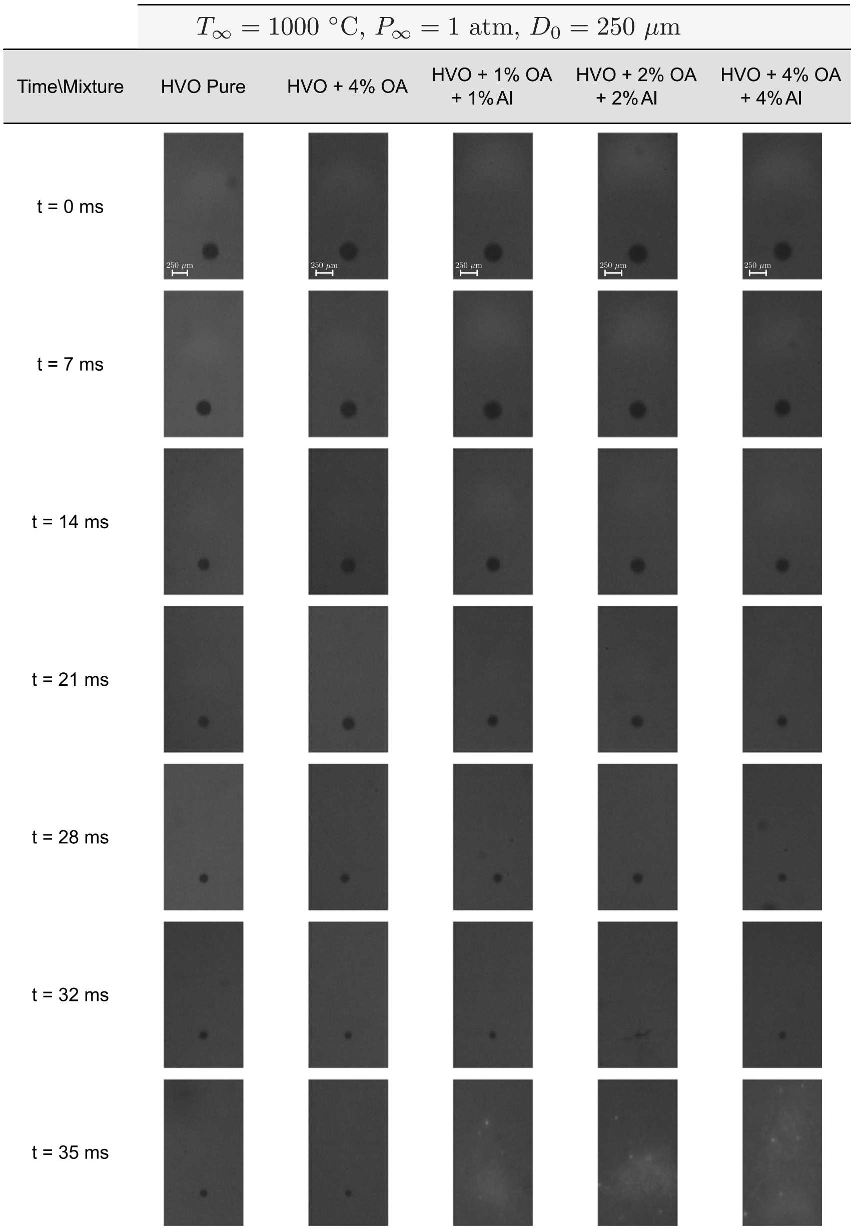

Fig. 12. Sequence of instantaneous images of the tested fuels at a furnace temperature of $T_\infty = 1000$ °C.

model modification.

$$B_{o,q} = \frac{\Delta h_c/\nu + c_{pg}\left(T_\infty - T_s\right)}{h_{fg,eff}} \tag{22}$$

As previously mentioned, in nanofuel droplet evaporation/combustion, particle accumulation during its process can potentially have a significant impact. According to the literature reviewed, agglomeration or aggregation of nanoparticles near the droplet surface creates a resistance for the liquid to evaporate, thus decreasing the burning rate. This effect is mainly felt in the last phase of the droplet lifetime, the so-called dry-out phase, where a shell of particles is formed, and evaporation occurs only when the liquid inside the shell reaches the outer surface through capillary action [16,57,58]. Although occurring on distinct time scales, this phenomenon resembles droplet drying, which is employed in diverse industries for solid particle formation and is well-established. Examples of such industries include pharmaceuticals [59,60]. A single droplet drying model was combined into the simplified single droplet combustion model previously described to obtain insights into the physical phenomena associated with particle agglomeration during combustion. It was based on the hypothesis developed by Mezhericher et al. [61] and later improved by Maurice et al. [62]. Due to slow particle diffusion, as the surface regresses, nanoparticles accumulate near the droplet surface [63], which eventually leads to a shell of particles [57]. This refers to the first drying phase ending and initiating the transition into the subsequent phase, known as the second drying phase [62]. During this phase, a shell of accumulated nanoparticles introduces a mass resistance that hinders the evaporation of the liquid fuel. As the evaporation progresses, the shell gradually thickens, causing a decrease in the evaporation rate. Ultimately, a critical point is reached. This occurs when the resistance of the shell becomes more significant than the compressive capillary forces applied to its surface, leading to a nearly constant diameter of the shell [61]. At this moment, the droplet enters the second drying phase. Subsequently, the shell of particles undergoes drying, promoting the nucleation of the residual liquid fuel presented within the droplet [64]. Consequently, the internal pressure of the droplet rises, ultimately leading to the disruptive burning phenomena [65]. The modeling and prediction of micro-explosions, more concretely aluminum particle

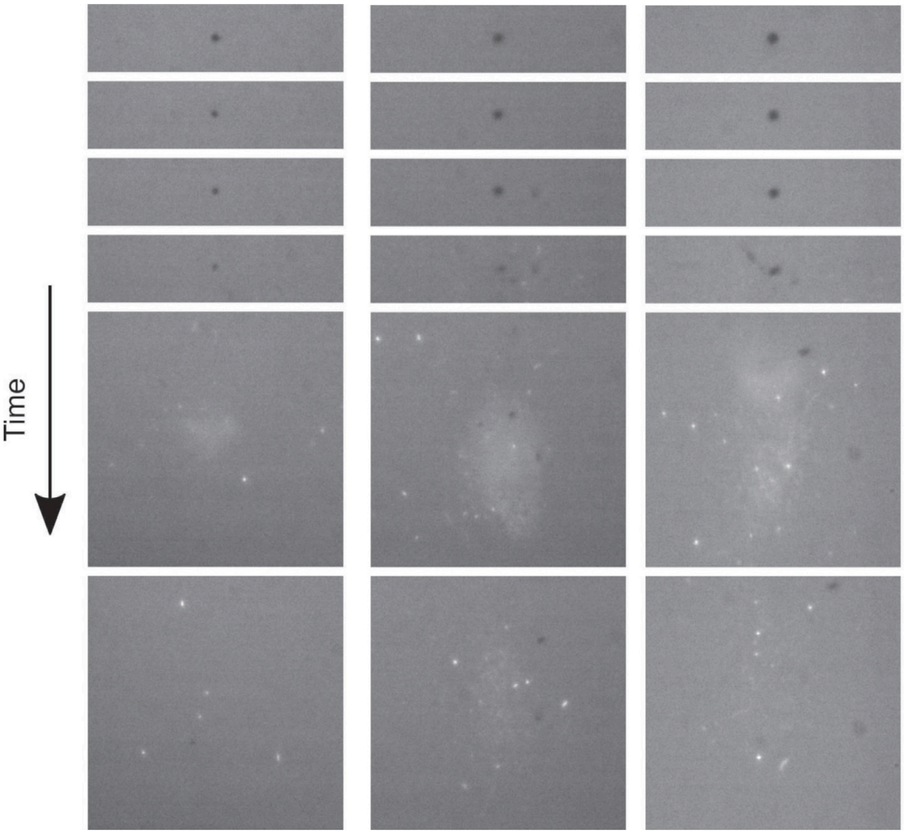

(a) (b) (c)

Fig. 13. Micro-explosions at $T_{\infty} = 800$ °C for different nanofuels: (a) HVO + 1% OA + 1% Al, (b) HVO + 2% OA + 2% Al, (c) HVO + 4% OA + 4% Al.

combustion that occurs at the end of the droplet lifetime, are beyond the scope of this study and will be investigated in future research. This theoretical model primarily focuses on the first drying phase since the outer diameter of the droplet remains relatively constant during the second drying phase. However, the transitional period between the first and second drying phases is incorporated in the model as part of the first drying phase. This decision is based on the ratio between the characteristic times of droplet evaporation and shell shrinkage and thickening, which includes the phenomenon of particle rearrangement of the shell formed on the droplet surface as it recedes, holds a theoretical value of approximately $\mathcal{O}(10)$ [61]. In the present mathematical model, the assumptions associated with the accumulation of particles in the droplet surface are related to the previous studies [61,62]. Initially, the analysis considers the radial symmetry of transport phenomena, aligning with the principles outlined in the D^2-law for droplet combustion. Additionally, intra-droplet circulation is disregarded, and it is assumed that spontaneous agglomeration of nanoparticles within the droplet does not occur. Moreover, all nanoparticles are assumed to be uniform in size and spherical. Based on these assumptions, the transport of nanoparticles within the droplet can be described using Fick second law [62]:

$$\frac{\partial Y_{np}(r,t)}{\partial t} = \frac{1}{r^2}\frac{\partial}{\partial r}\left(r^2 \mathcal{D}_{pl}\frac{\partial Y_{np}}{\partial r}\right) \tag{23}$$

for $0 \leq r \leq r_s(t)$, where Y_{np} is the volume fraction of nanoparticles and $\mathcal{D}_{pl}$ is the diffusivity coefficient of particles in liquids, which can be calculated from Einstein–Stokes relation [57]

$$\mathcal{D}_{pl} = \frac{k_B T_l}{6\pi \mu_l r_p} \tag{24}$$

where k_B is the Boltzmann constant, T_l and μ_l are, respectively, the liquid temperature and dynamic viscosity and r_p is the particle radius. For the initial condition of Eq. (23), it is assumed that initially, the nanoparticles inside the droplet are spherical and uniformly distributed so that

$$Y_{np}(r, t=0) = Y_{np,o}(r)\,, \tag{25}$$

where $Y_{np,o}$ is the initial volume fraction of nanoparticles in the nanofuel mixture. The corresponding boundary conditions are [62]

$$\frac{\partial Y_{np}(r,t)}{\partial r} = 0 \quad r = 0 \tag{26a}$$

$$\frac{\partial}{\partial t}\left[\int_0^{r_s(t)} Y_{np}(r,t)\rho_{np} 4\pi r^2 dr\right] = 0 \quad r = r_s(t) \tag{26b}$$

where ρ_{np} is the density of the nanoparticles material. The first boundary condition is due to the spherical symmetry of the problem, and the second one describes the conservation of overall solid mass within the droplet, as the nanoparticles are considered to remain in the droplet interior during the evaporation process [61]. Based on the species volume fraction within the droplet, it becomes apparent that a specific instant exists when the solid content attains a saturation value on the droplet surface [62]. In this study, the saturation value was assumed to be $Y_{np,max} = Y_{np,sat} = 0.6$, indicating the maximum theoretical value for orthorhombic packing of mono-sized spheres [66]. This particular point, commonly referred to as the “locking point” [61,62], means the onset of agglomeration among the nanoparticles that were previously independent. As a result, a thin shell composed of connected solid particles is formed through intermolecular attractive forces [62]. This moment marks the initiation of the transition period.

When the transition starts, a thin layer of nanoparticles is submerged while the liquid evaporates from the surface until the agglomerated particles are exposed to the surrounding gas [62]. At this stage, both internal and external pressures act on the droplet. The internal

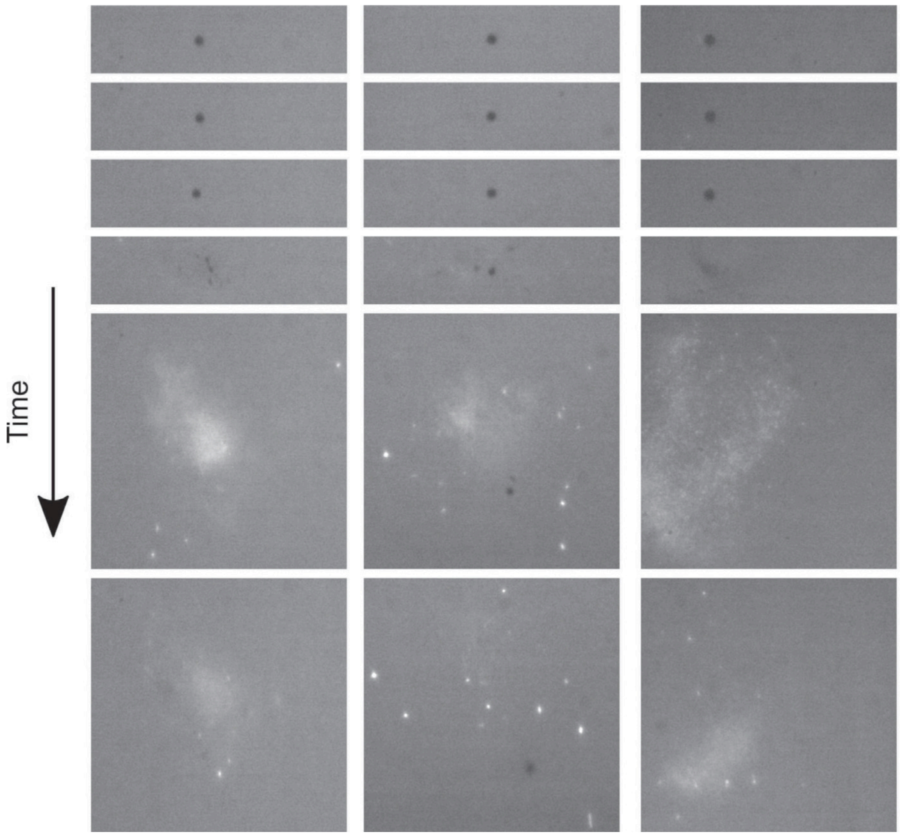

(a) (b) (c)

Fig. 14. Micro-explosions at $T_\infty = 1000$ °C for different nanofuels: (a) HVO + 1% OA + 1% Al, (b) HVO + 2% OA + 2% Al, (c) HVO + 4% OA + 4% Al.

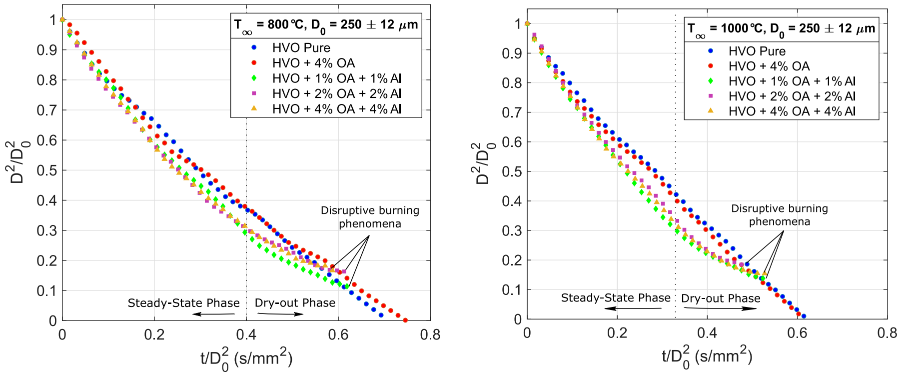

(a) (b)

Fig. 15. Droplet size evolution of pure HVO, HVO with the addition of 4.0 wt.% of OA and the different nanofuels studied for: (a) $T_\infty = 800$ °C. (b) $T_\infty = 1000$ °C.

pressure of the droplet counteracts the external pressure, reducing the capillary compression effect to some extent [62]. The development of the mathematical expressions for those pressures is elaborately described in [61]. In the present work, only the final expressions will be presented for simplification purposes. Consequently, the external pressure exerted on the shell is caused by both capillary effects and interfacial tension of the liquid and which is given by [61,62]

$$P_{ext}(t) = 2\gamma_{lv}\cos(\theta)\left[\frac{3}{2r_p}\left(\frac{1-\varepsilon}{\varepsilon}\right)+\frac{1}{r_s(t)}\right] \tag{27}$$

where γ_{lv} is the liquid fuel surface tension at T_s; θ is the contact angle, i.e., the angle where the liquid–vapor interface meets the solid surface; and ε is the shell porosity, $\varepsilon = 1 - Y_{np,sat} = 0.4$ [66]. The liquid fraction primarily influences the internal pressure exerted on the shell. Once the shell is formed, the pressure within the droplet does not undergo instantaneous changes but rather maintains the same value as the internal pressure before shell formation [61]. The evaluation of the internal pressure within the droplet follows the Laplace–Young equation and is expressed by [61,62]

$$P_{int}(t) = \frac{2\gamma_{lv}}{r_s(t)}\,. \tag{28}$$

Considering the shell of agglomerated nanoparticles as a pseudo-continuous solid body, the radial and tangential mechanical stresses

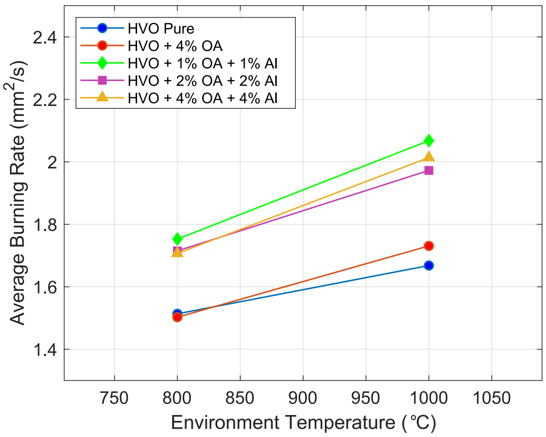

Fig. 16. Average droplet burning rate for the steady-state combustion phase ($D^2/D_0^2 > 0.3$) of pure HVO, HVO with the addition of 4.0 wt.% of OA and the different nanofuels studied as a function of the furnace temperature.

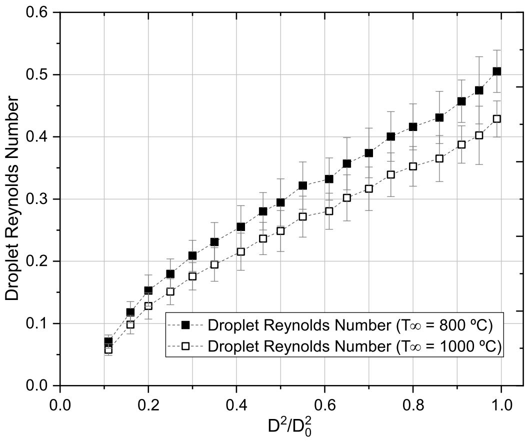

Fig. 17. Droplet Reynolds Number as a function of the droplet squared ratio at furnace temperatures of $T_\infty = 800$ °C and $T_\infty = 1000$ °C.

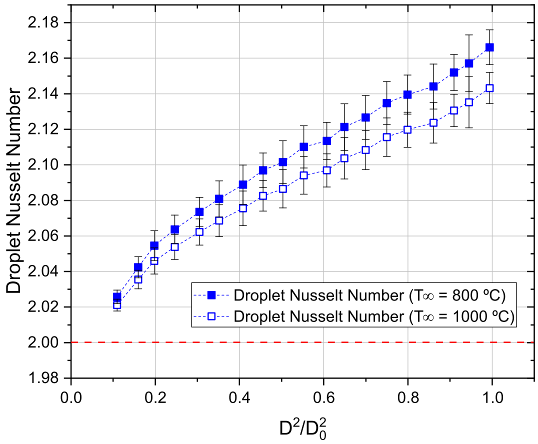

Fig. 18. Droplet Nusselt Number as a function of the droplet squared ratio at furnace temperatures of $T_\infty = 800$ °C and $T_\infty = 1000$ °C. (For interpretation of the references to color in this figure legend, the reader is referred to the web version of this article.)

within this spherical shell caused by internal and external pressures can be approximated by [61,62]

$$\sigma_r(r) = \frac{P_{ext} b^3 \left(r^3 - a^3\right)}{r^3 \left(a^3 - b^3\right)} + \frac{P_{int} a^3 \left(b^3 - r^3\right)}{r^3 \left(a^3 - b^3\right)} \tag{29}$$

Table 4
Continued estimated magnitude order from experimental results.

Parameters	Order of magnitude ($\mathcal{O}$)
K_c	10^{-6} m^2 s^{-1}
k_B	10^{-23} J K^{-1}
T_l	10^3 K
μ_l	10^{-2} Pa s
r_p	10^{-8} m
D_{pl}	10^{-10} m^2 s^{-1}
Pe	$10^3 \gg 1$

$$\sigma_\psi(r) = \frac{P_{ext} b^3 \left(2r^3 + a^3\right)}{2r^3 \left(a^3 - b^3\right)} - \frac{P_{int} a^3 \left(2r^3 + b^3\right)}{2r^3 \left(a^3 - b^3\right)} \tag{30}$$

for $a \le r \le b$, where a and b are, respectively, the inner and outer radii of the shell. On the outer surface of the shell, the presence of capillary effects causes additional compressive capillary forces performing tangentially on the nanoparticles [61]. In the case of a liquid bridge formed between two spherical particles, as depicted in Fig. 7, these additional compressive capillary forces contribute towards the tangential stress experienced at the droplet surface [61,62]. Where α is the half-filling angle and L and ρ are the principal radii of the liquid meniscus. In this work it was assumed that $\theta = 30°$, $\alpha = 45°$ and $\rho = \infty$, so that $L = r_p \sin(\alpha)$.

The condensed shell containing agglomerated nanoparticles undergoes collapse or rearrangement due to droplet evaporation, provided that the following buckling criterion is fulfilled [61,62].

$$\max\left(\left|\sigma_r\right|, \left|\sigma_\psi\right|\right) > \sigma_y \tag{31}$$

Here, σ_y represents the yield stress of the shell. Since the literature does not provide an available value for σ_y of the agglomerated nanoparticle shell, and its direct measurement would be highly challenging, this parameter must be determined by fitting with experimental findings.

Following the collapse of the shell, this iterative process continues until the shell attains a sufficient thickness to suffer the capillary pressure, resulting in no agreement of the buckling criterion defined by Eq. (31) [62]. The repeating process of evaporation and shell collapse, which characterizes the transition period, is well explained in [61]. The point at which the buckling criterion is not achieved determines the end of the transition period and the onset of the second drying phase, where the outer diameter of the droplet remains constant until a micro-explosion occurs. Consequently, following the initial droplet shrinkage primarily governed by the D^2-law, considering the radiation effects, the further reduction in droplet size ceases due to constraints imposed by particle packing.

$$\frac{dD^2}{dt} = 0 \tag{32}$$

The relative motion of the regressing droplet surface and the nanoparticles can be assessed by comparing the time scales, which can be quantified using the Péclet number [57].

$$Pe = \frac{K_c}{8D_{pl}} \tag{33}$$

Consequently, during the evaporation process, nanoparticles have insufficient time to diffuse and are quickly included on the regressing droplet surface, as shown in Table 4 [57]. Hence, it can be assumed that the diffusion of nanoparticles in the liquid is negligible.

This significantly simplifies the way of determining the species concentration profile within the droplet, as now one merely has to determine the amount of nanoparticles dragged inward by the recessing droplet surface. Therefore, instead of solving Eq. (23), the volume fraction of nanoparticles inside the droplet was obtained in a simplified manner, both in time and in the radial direction. To better understand this approach, Fig. 8 shows the volume fraction profile of nanoparticles within the droplet. It divided the initial droplet radius into radial

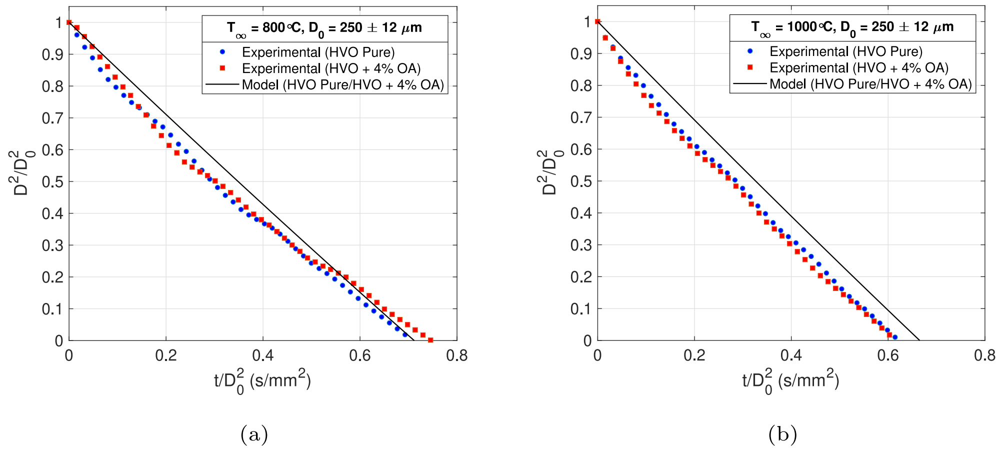

Fig. 19. Comparison between experimental and numerical results for the droplet size evolution of pure HVO and HVO with the addition of 4.0 wt.% of OA at (a) T_∞ = 800 °C, (b) T_∞ = 1000 °C.

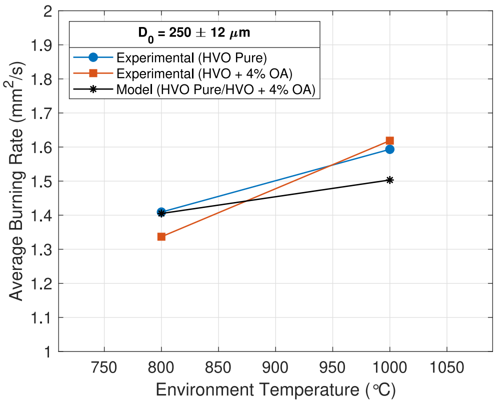

Fig. 20. Comparison of average burning rate for experimental and numerical approaches at both furnace temperature: T_∞ = 800 °C and T_∞ = 1000 °C.

shells of the same thickness Δr. As the evaporation progresses, the nanoparticles near the droplet surface are integrated into the closest radial shell to the regressing droplet surface until the saturation point is achieved and the transition period begins. Afterward, the nanoparticles are included in the two closest radial shells to the surface, and so on, increasing the number of radial shells that include dragged nanoparticles and, therefore, increasing the thickness of the shell of agglomerated nanoparticles.

Time step and grid studies were performed. Subsequently, a time step $\Delta t = 1 \cdot 10^{-5}$ s was considered, and grid analysis showed that by discretizing the droplet radius into 1000 radial shells, i.e., for a radial shell thickness of $\Delta r = 1.25 \cdot 10^{-7}$ m, grid independence was achieved.

3. Results and discussion

3.1. Experimental results

Extensive investigations have been conducted on the combustion of nanofuel droplets with relatively lower particle concentrations, as evidenced by previous studies [4,14]. Consequently, this section will be dedicated to the discussion of the findings from experimental and numerical approaches for the combustion of pure HVO, HVO + OA (4.0 wt.%), and three different nanofuels (1.0 wt.%, 2.0 wt.%, and 4.0 wt.%). The experiments using a surfactant-to-nanoparticle mass ratio of 1:1, and the furnace temperatures of T_∞ = 800 °C and T_∞ = 1000 °C were performed. Before evaluating the combustion of the nanofuel droplets, it is essential to evaluate the combustion characteristics of pure HVO droplets as a baseline for comparison. Furthermore, the highest concentration of surfactant (4.0 wt.%) used to enhance the stability of nanofuel was also tested to better identify nanoparticle influence. It is relevant to mention that the droplet size evolution of each fuel was not acquired for the heating phase due to the optical limitations of the experimental setup. The droplet autoignition occurs when the droplet leaves the injector tip and is susceptible to high temperatures [4].

Results show the droplet combustion of pure HVO and HVO + 4.0 wt.% OA for both furnace temperatures is in good agreement with the D^2-law, without the existence of disruptive behavior phenomena, as shown in Figs. 9 and 10. The combustion of pure HVO was explained in detail in a preliminary study [14], displaying a reduction of the droplet diameter as time evolves, being more explicit at the higher furnace temperature. The visualization of the pure HVO combustion is also presented in [14]. Additionally, the droplet size evolution of HVO + 4.0 wt.% OA practically overlaps with the temporal history of the diameter squared of pure HVO for both furnace temperatures. This outcome is highly promising since adding small concentrations of OA significantly increases the stability of nanofuels without jeopardizing the burning characteristics of HVO. This result concurs with the findings reported by Javed et al. [20,21]. The authors investigated the impact of adding small concentrations of OA to n-heptane and kerosene droplets at high temperatures and stated that such additions did not significantly influence the combustion behavior when compared to pure fuels.

As aforementioned, 40 droplets were required to produce a droplet size evolution for each fuel and a five-point moving average was employed to smooth all the D^2-law curves [4]. Moreover, it should be stated that, for diameters below $D^2/D_0^2 = 0.1$ it was not possible to accurately determine the droplet diameter for each droplet size evolution curve presented in this study. Therefore, droplet size evolution values from that point on were obtained via the best-fit trend line. For the experimental results of pure HVO and HVO + 4.0 wt.% OA displayed in Figs. 9 and 10.

As stated, a high-speed camera with a high-magnification lens was used to rigorously capture the combustion process and identify potential disruptive burning phenomena. In addition, to ease the comprehension of the qualitative results provided by the combustion of the different fuels, a sequence of instantaneous images of falling burning droplets at T_∞ = 800 °C and T_∞ = 1000 °C is exhibited in Figs. 11 and 12. The frame where ignition occurs is defined as t = 0 ms, with a droplet diameter of approximately 250 µm.

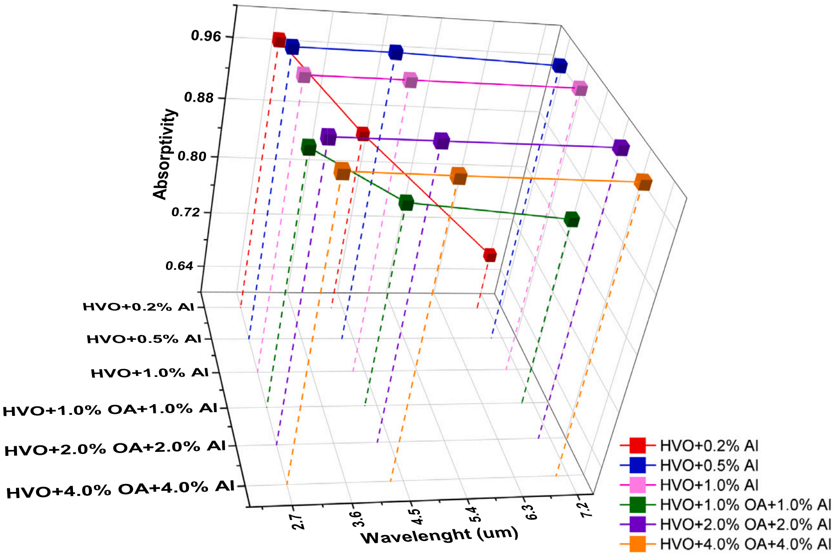

Fig. 21. Absorptivity as a function of wavelength for each fuel.

The flame of the droplet exhibits a low luminous intensity, primarily attributed to the minimal presence of aromatic compounds in the HVO fuel [14]. The visualization reveals that regardless of the furnace temperature, only including nanoparticles as an additive leads to disruptive burning phenomena. Pure HVO and HVO + 4.0 wt.% OA does not display any puffing or micro-explosion during the droplet lifetime. However, all the nanofuels studied exhibited micro-explosions with an occurrence rate of 100% at the end of their lifetime, regardless of the experimental conditions and particle concentration, as already noticed [4,14]. These phenomena are exclusively observed when nanoparticles are introduced, strongly suggesting their active involvement in driving its occurrence. At the initial stage, when the droplet enters the quartz tube, it is exposed to high temperatures, and the liquid phase starts to evaporate. In this stage, the nanoparticles remain inside the droplet since no ejections are identified during the main course of the combustion. Subsequently, the concentration of the solid phase increases and begins preferentially at the droplet surface where mass and heat exchange occurs. Consequently, a shell is forming, becoming more resistant to the compressive capillary forces induced by the regression of the droplet surface. At some point, the shell strength overcomes the compressive stress, which ceases shell shrinkage. During this procedure, the shell is heated up, hence the droplet temperature exceeds the boiling point of the liquid fuel. This promotes nucleation of the liquid fuel that remains inside the shell of particles [67]. As a result, the pressure inside the structure increases, ultimately prompting the shell to disintegrate, promoting the appearance of disruptive burning phenomena. Later, the final residue is aggressively projected away, eventually ascending as the smoke tail occuring from the aluminum combustion. Figs. 13 and 14 show the sequence of images of disruptive burning phenomena displayed in nanofuel droplet combustion for each particle concentration at $T_\infty = 800$ °C and $T_\infty = 1000$ °C, respectively.

This sequence of images enables a more comprehensive visualization of the disruptive burning events, providing detailed insights of their behavior. At the end of the droplet lifetime, identifying these events is noticeable when a droplet expansion occurs. This phenomenon is denominated as puffing. After a small cluster of nanoparticles is expelled from the main droplet, these ignite immediately and turn into several bright spots that characterize the aluminum combustion. Droplet expansion preceding its explosion was repeatedly observed.

It is worth noting that these two types of disruptions are independent of the experimental conditions since were observed for each particle concentration and furnace temperature. Although the behavior of micro-explosions exhibited some stochasticity, it was possible to identify the most typical occurrences for each experimental condition. Concerning the influence of particle concentration on micro-explosion phenomena, the results seem to indicate that increasing the particle concentration enhances the intensity of micro-explosions at both furnace temperatures, as will be explored in future studies. The micro-explosion intensity is related to the number of fragments expelled from the primary droplet, according to the appearance of small luminous spots indicative of aluminum combustion [68]. The occurrence of micro-explosions has a notable impact not only on the duration of the droplet lifetime but also on atomization, as it enhances the dispersion of the solid phase. Unfortunately, the available experimental setup does not facilitate collecting combustion residues or measuring heat released by nanoparticles. These aspects are crucial for evaluating their impact on emissions and potential damage to the combustion chamber. Developing a nanofuel spray combustion system would be beneficial to comprehensively assess the effective potential of nanofuels.

After introducing the qualitative results, the analysis of the droplet size evolution for nanofuel droplets is displayed in Fig. 15. Additionally, the normalized temporal history of the diameter squared of pure HVO and HVO with the addition of 4.0 wt.% OA is also presented in Fig. 15.

The quantitative results suggested that the addition of aluminum nanoparticles to HVO results in a departure from the D^2-law. The nanofuel droplet combustion displayed four different combustion phases: (i) a classical steady-state phase; (ii) a dry-out phase, perceived at $D^2/D_0^2 \approx 0.3$; (iii) a disruptive behavior phase, followed by (iv) a particle combustion phase, characterized by the appearance of bright spots, indicating the combustion of aluminum, as previously mentioned. The identification of the dry-out phase was determined based on a decrease in the reduction rate of the droplet diameter, as depicted in Fig. 15.

Moreover, these micro-explosions were more intense for higher particle concentrations and furnace temperatures. Furthermore, adding aluminum nanoparticles to HVO increases the droplet burning rate during steady-state combustion compared to pure HVO and HVO + 4.0 wt.% of OA regardless of particle concentration and furnace temperature conditions. However, it should be pointed out that all the nanofuels presented a similar droplet size evolution for identical furnace conditions, regardless of the nanoparticle concentration. This observation is particularly significant in clarifying the relation between particle concentration and radiation absorption. The enhanced

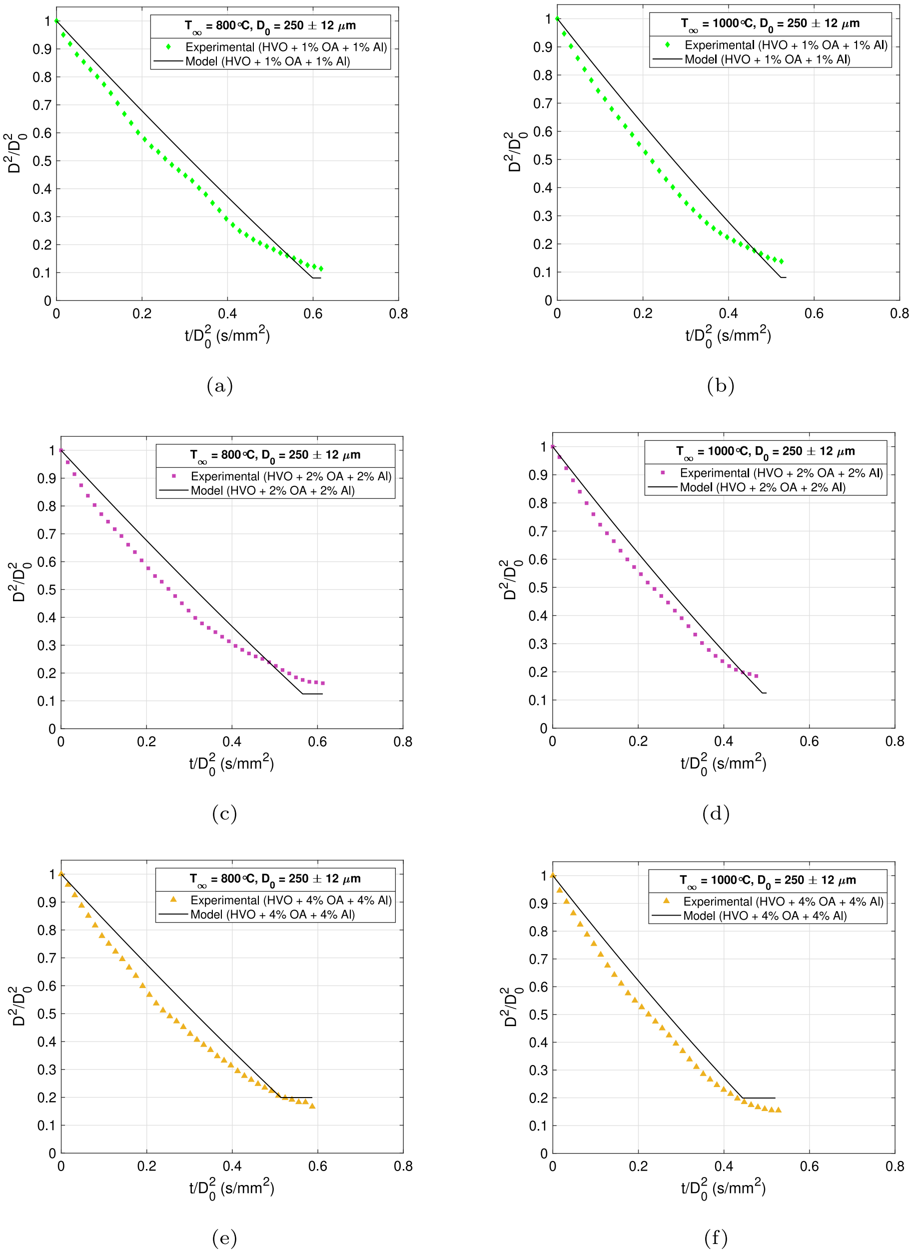

Fig. 22. Comparison between experimental and numerical data for the droplet size evolution of (a) HVO+1% OA+1% Al ($T_\infty = 800$ °C), (b) HVO+1% OA+1% Al ($T_\infty = 1000$ °C), (c) HVO+2% OA+2% Al ($T_\infty = 800$ °C), (d) HVO+2% OA+2% Al ($T_\infty = 1000$ °C), (e) HVO+4% OA+4% Al ($T_\infty = 800$ °C), (f) HVO+4% OA+4% Al ($T_\infty = 1000$ °C).

burning rate in nanofuels can be attributed to the increased radiation absorption by the droplets, as will be examined later. Based on this, the findings suggest that at a particle concentration of 1.0 wt.%, the droplet exhibits significant radiation energy absorption. Consequently, further increasing the nanoparticle quantity does not induce significant enhancements. Adding a minimal concentration of 1.0 wt.% aluminum nanoparticles leads to a substantial increase in the burning rate during the prolonged combustion phase, a noteworthy reduction in droplet lifetime, and improved suspension and long-term stability of nanoparticles in the base fuel. Furthermore, these effects reduce equipment wear, making it a promising approach for practical applications. Besides that, reduced quantities of particles are required to produce nanofuels more cost-effective, a crucial variable when considering their viability for real-world applications. The maximum standard deviation for all curves featured in Fig. 15(a) is 0.0038 mm^2/mm^2, and for all curves depicted in Fig. 15(b) it is 0.0063 mm^2/mm^2. As already mentioned, an approximately initial diameter of 250 μm was considered, and the influence of viscosity variation was accounted for in the standard deviation.

For comparison purposes, Fig. 16 displays the average burning rates of pure HVO, HVO + 4.0 wt.% OA and the different nanofuels for the two different temperature conditions studied. To correctly investigate the enhancement in the droplet burning rate, this was calculated using its average value and disregarding the dry-out phase, i.e., for $D^2/D_0^2 < 0.3$.

The burning rate, K_c was determined from the droplet diameter history curves using the following expression, adapted from Eq. (5):

$$K_c = -\frac{dD^2}{dt} \tag{34}$$

Instead of displaying the droplet burning rate as a function of time, it was defined to present the average burning rate, as given the circumstances, the latter introduces much more useful information regarding the burning behavior of isolated droplets. For the pure HVO

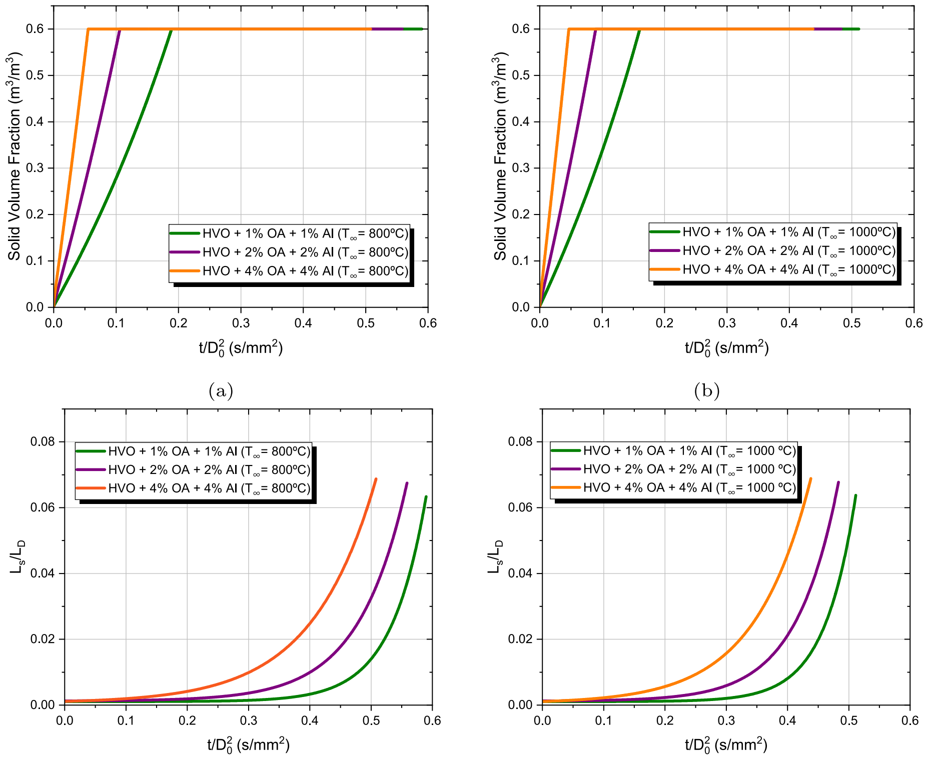

(a) (b)

(c) (d)

Fig. 23. Solid Volume Fraction at (a) $T_\infty = 800$ °C, (b) $T_\infty = 1000$ °C, and shell thickness and droplet radius ratio at (c) $T_\infty = 800$ °C, (d) $T_\infty = 1000$ °C.

and HVO + 4.0 wt.% OA, regardless of the furnace temperature, the maximum standard deviation is 0.334 mm^2/s and 0.369 mm^2/s, respectively. For the nanofuels, the maximum standard deviation for the burning rate is 0.463 mm^2/s. As can be noticed, the improvement in the burning rate is more notorious for higher furnace temperatures related to more radiation energy being transmitted from the DTF walls. This observation is in accordance with the droplet size evolution previously presented.

The experimental findings presented in this study provide valuable support for developing a mathematical model to evaluate the droplet size evolution and burning rate. To this end, Fig. 17 includes data on droplet Reynolds number, an essential parameter in characterizing the droplet behavior and combustion process.

To determine the droplet Reynolds number, Re$_d$, Eq. (11) was employed. The measured velocity of the droplets and the airflow velocity, U_∞, displayed in Table 2 was used to evaluate the droplet relative velocity, U$_{rel}$, for the experimental conditions. Accordingly, the gas kinematic viscosity, ν_g was estimated at the mean temperature $\overline{T}_2 = \left(T_f + T_\infty\right)/2$, for the gaseous region outside the flame front [48]. Fig. 17 displays the droplet Reynolds number as a function of D^2/D_0^2 for furnace temperatures (a) $T_\infty = 800$ °C and (b) $T_\infty = 1000$ °C. This finding indicates a decrease in the droplet Reynolds number as the droplet diameter decreases. Additionally, air viscosity increases with temperature, and higher values of T_∞ further reduce the droplet Reynolds number. Notably, the estimated droplet Reynolds number values remain relatively low due to the experimental conditions involving small initial droplet diameters and high-temperature environments. As reported by [53], for Re$_d \leq 2$, no separation effects are noticed. Consequently, in the present study, this phenomenon is negligible. Regarding the flame characteristics, Pandey et al. [69] proposed a flame regime map that enables the classification of the flame behavior, ranging from an envelope flame to a wake structure, by considering the droplet Reynolds number. Considering that the Reynolds number relies on the range of $0 <$ Re$_d < 5$, it was confirmed that the burning process would be characterized by an envelope flame surrounding the droplet. At last, to quantify the convective effects on the burning droplets, the droplet Nusselt number, Nu$_d$, was determined employing Eq. (36). The gas Prandtl number, Pr$_g$, was evaluated at $\overline{T}_2$ [48]. Fig. 18 depicts Nu$_d$ as a function of D^2/D_0^2 for (a) $T_\infty = 800$ °C and (b) $T_\infty = 1000$ °C, where the red dashed line corresponds to Nu$_d$ = 2, a case where there is no convection. The results suggest that the droplet Nusselt number decreases with increasing air temperature and the decrease of the droplet diameter. Moreover, it can be concluded that the experimental study was performed under weak, forced convection in a laminar regime.

3.2. Modeling results

The performance of the mathematical model was initially assessed for pure HVO. The experimental analysis showed no substantial differences in the combustion process in pure HVO and HVO with 4.0 wt.% OA. Thus, the influence of OA addition was neglected in the mathematical model. Consequently, the properties of both liquid fuels were approximated to those of n-hexadecane, as previously mentioned. Fig. 19 shows the droplet size evolution of pure HVO and HVO + 4.0 wt.% OA for experimental and numerical data. The lower and higher furnace temperature results are displayed in Fig. 19(a) and (b), respectively. The prediction of the combustion of pure HVO and HVO + 4.0 wt.% OA was performed assuming n-hexadecane as a surrogate fuel to estimate the combustion dynamics and the incorporation of the convective effects.

Regardless of the furnace temperature, the mathematical model predicts droplet size evolution evidencing a linear droplet diameter reduction as time evolves. The model accurately predicts the behavior at $T_\infty = 800$ °C. However, the model overpredicts the droplet diameter variation for higher temperatures compared to the experimental results. The average burning rate for experimental and numerical data was analyzed for comparison purposes. Fig. 20 shows the influence of the furnace temperature on the average burning rate for experimental and numerical results. Accordingly, for both approaches, the average burning rate increased with the furnace temperature, and better performance of the mathematical model was observed for the T_∞ = 800 °C.

A sensibility analysis was performed, focusing on potential uncertainties regarding the estimation of model parameters. This analysis aimed to assess the robustness of the model by examining the substantial variations of these parameters in average droplet burning rates under the two furnace temperatures. The sensibility analysis for fuel gas thermal conductivity, k_F, and the fuel gas heat capacity, c_{pF}, is presented in Appendix D. In light of this, it can be affirmed that the model exhibits robustness within the scope of this study, hence can accurately replicate the underlying physical phenomena that occur during the combustion of isolated liquid fuel droplets, thereby validating its reliability. Following the validation of the model and the discussion of the results for pure liquid fuels, numerical simulations were carried out considering the addition of nanoparticles. For nanofuels predictions, the gas domain analysis remains unchanged compared to pure liquid, including the effects of nanoparticle addition in terms of radiation absorption and particle agglomeration. The nanoparticles are considered insoluble with uniform size and distribution. The radiation absorption incorporates the absorptivity of each fuel, allowing a more accurate representation of the energy transfer mechanisms in the nanofuel combustion process. The emissivity is considered equal to 1, and the absorptivity is shown in Fig. 21 as a function of the wavelength. For a more detailed analysis, nanofuels with lower particle concentrations (0.2, 0.5, 1.0 wt.%) were also evaluated [4]. The results show that increasing the particle concentration increases the absorptivity. On the other hand, increasing the wavelength decreases the absorptivity, regardless of the particle concentration.

As previously mentioned, the absorptivity results were acquired using a FTIR, and a pathlength of 1 μm was considered. This value was determined based on previous investigations, indicating that liquid samples typically have a short optical pathlength with an order of magnitude of microns (μm) [70–72]. Similar to the fuel gas thermal conductivity and heat capacity, a sensibility analysis focused on the influence of the absorptivity concerning the pathlength was conducted and is displayed in Appendix D. Briefly, for the simulations, a wavelength of $\lambda = 2.7$ μm and an optical pathlength of 1 μm were selected, producing the most accurate agreement with the experimental data. Regarding the particle aggregation, the yield stress of the shell, σ_y = 10 MPa, was determined by fitting with the experimental results. That being said, Fig. 22 shows the numerical results obtained for the droplet size evolution for each nanofuel at the two furnace temperatures.

Furthermore, experimental data were included to compare and validate the results. Fig. 22 shows the numerical results at the steady-state and dry-out phase, where the latter indicates a constant diameter at the end of the droplet lifetime. In this context, the nanofuel predictions exhibit a steeper and more abrupt transition between the steady-state and dry-out phase in contrast to the experimental observations, where this transition appears to be more smoother. This observation is a consequence of the assumption performed by the model applied, pointing out that the transition between phases occurs without any mass resistance arising from the formation of the shell of nanoparticles at the droplet surface. Further research into this transition would be relevant to achieve better accuracy in the model results. In addition, the results show that increasing the particle concentration increases the dry-out phase which may be attributed to the fact that the nanoparticles remain within the droplet during the combustion process. Thus, an increased particle concentration corresponds to a higher solid phase during the final phase of the droplet lifetime. The simplified model predictions reasonably agreed with the experimental results. However, it should be stated that the model slightly underpredicted the droplet burning rate during the steady-state phase for all nanofuels investigated. To better understand this observation, Table 5 shows the average burning rate enhancement for experimental and numerical results regarding all the nanofuels. This analysis is related to the steady-state phase ($D^2/D_0^2 > 0.3$) for both furnace temperatures. The results obtained from both experimental and numerical approaches indicate a similarity in its magnitude which is observed for both furnace conditions. In particular, these results evidence that the enhanced droplet burning rate resulting from adding aluminum nanoparticles can be primarily attributed to radiation absorption by the nanofuel droplet. This effect is more noticeable at a higher furnace temperature, as can be seen in Appendix E. On the other hand, the increasing of particle concentration only produces a slight increase in the burning rate. Nevertheless, it should be noted that other mechanisms may produce a minor influence on the observed increase in droplet burning rate.

Table 5

Average burning rate enhancements results from experimental and numerical data for the steady-state phase until $D^2/D_0^2 > 0.3$ in respect to the pure HVO.

Nanofuels	Average burning rate enhancement			
	T_∞= 800 °C		T_∞ = 1000 °C	
	Experimental	Model	Experimental	Model
HVO + 1% OA + 1% Al	15.1%	9.9%	22.9%	20.5%
HVO + 2% OA + 2% Al	12.6%	10.5%	17.2%	20.1%
HVO + 4% OA + 4% Al	12.1%	10.5%	19.7%	20.1%

To gain more insights into the numerical model, the evolution of the solid volume fraction inside the droplet during the combustion process was performed. Fig. 23 shows the model predictions on the evolution of the solid volume fraction inside the droplet for the nanofuels studied (a) at T_∞ = 800 °C and (b) T_∞ = 1000 °C. Additionally, a relation between the shell thickness with respect to the droplet is provided during the combustion process with an exponential fitting, as shown in Fig. 23(c) for T_∞ = 800 °C and (d) T_∞ = 1000 °C. The results reveal that the maximum solid volume fraction is achieved at an earlier stage when the particle concentration is higher, regardless of the furnace temperature. Besides that, the shell at the beginning of the second drying stage is predicted to be thicker for a higher initial particle concentration. The model estimated that for the beginning of the second drying stage, the shell thickness was approximately 2.6 μm for the nanofuel with 1 wt.% of aluminum nanoparticles, 3.4 μm for the nanofuel with 2 wt.% of aluminum nanoparticles and 4.1 μm for the nanofuel with 4 wt.% of aluminum nanoparticles.

Overall, the simplified model could accurately reproduce the combustion characteristics of nanofuel droplets. As a result, it provided valuable insights into the underlying physical processes, enhancing the understanding that contributes to the broader knowledge of nanofuel combustion phenomena. Further research on predicting the disruptive burning phenomena and multi-component physics should be explored to understand the nanofuel combustion phenomena better.

4. Conclusions

The present work evaluated the effect of adding aluminum nanoparticles on the combustion characteristics of HVO in experimental and numerical approaches. Droplet combustion experiments and the development of a simplified macroscopic model were performed, and the key findings of this study are summarized below:

- The addition of surfactant to a nanofuel significantly enhances the stability, enabling experiments to be conducted with higher particle concentrations. In terms of physical properties, adding oleic acid and aluminum nanoparticles significantly affects the viscosity, being more evident for the highest particle concentration. On the other, variations in the density and surface tension are negligible.

- The experiments showed that pure HVO and HVO + 4% OA burns as a liquid fuel and are in good agreement with the D^2-law. In addition, the combustion behavior including 4% OA to HVO is practically disregarded.
- Adding aluminum nanoparticles to the HVO and oleic acid causes a deviation from the D^2-law. Disruptive burning phenomena and particle combustion are noticed at the end of the droplet lifetime for all nanofuels. Their intensity increased with particle concentration and furnace temperature.
- The addition of aluminum nanoparticles to HVO increased the average droplet burning rate, being more pronounced for higher furnace temperatures. However, the increase in the overall droplet burning rate showed no particular dependence on particle concentration.
- Regarding the numerical results, n-hexadecane was employed as a surrogate fuel, and the incorporation of the convection effects indicated a satisfactory prediction of the combustion of pure HVO and HVO + 4% OA.
- Modeling results indicate that radiation absorption plays a relevant role in nanofuel droplet combustion. This mechanism is responsible for the increased droplet burning rate. The results suggest that regardless of the particle concentration, the absorptivity is approximately equal to 1, assuming that the aluminum nanoparticles behave as a blackbody. Furthermore, the model predicts the final droplet diameter before the occurrence of disruptive burning phenomena being larger for higher particle concentration.

CRediT authorship contribution statement

Inês A.S. Ferrão: Writing – original draft, Visualization, Investigation, Formal analysis. **Tomás S.M. Mendes:** Visualization, Investigation, Formal analysis, Data curation. **Miguel A.A. Mendes:** Writing – review & editing, Supervision, Software, Resources, Methodology, Investigation. **Ana. S.O.H. Moita:** Writing – review & editing, Supervision, Resources, Methodology, Funding acquisition, Conceptualization. **André R.R. Silva:** Writing – review & editing, Supervision, Resources, Project administration, Methodology, Funding acquisition.

Declaration of competing interest

The authors declare that they have no known competing financial interests or personal relationships that could have appeared to influence the work reported in this paper.

Data availability

Data will be made available on request.

Acknowledgment

Inês A. S. Ferrão acknowledges Fundação para a Ciência e Tecnologia (FCT), Portugal for the provision of Ph.D scholarship with the reference SFRH/BD/144688/2019. The present work was performed under the scope of the Laboratório Associado em Energia, Transportes e Aeronáutica (LAETA) and Laboratório de Robótica e Sistemas de Engenharia (LARSyS) activities through the projects 10.54499/UIDB/50022/2020, 10.54499/UIDP/50022/2020, 10.54499/UIDB/50009/2020, 10.54499/UIDP/50009/2020 and 10.54499/LA/P/0079/2020. The authors acknowledge Fundação para a Ciência e Tecnologia, Portugal for partially financing the research through project PTDC/EMETED/7801/2020. A.S. Moita also acknowledges FCT, Portugal for partially financing her contract through CEECINST/00043/2021/CP2797/CT0005, doi: 10.54499/CEECINST/00043/2021/CP2797/CT0005.

Fig. 24. Experimental setup (front view) from [14].

Appendix A. Experimental setup

See Fig. 24.

Appendix B. Physical properties

B.1. n-Hexadecane (C_{16} H_{32})

The gas thermal conductivity and heat capacity curves of n-hexadecane as a function of temperature were only available for 1000 K and 1500 K, respectively. Consequently, they were extrapolated up to 2000 K using the Excel forecast sheet. These extrapolations are graphically represented in the Fig. 25

Appendix C. Mathematical model

C.1. Incorporation of the convective effects

To incorporate the effects of forced convection into the droplet combustion model, the formulation presented in [31] was adopted. The approach is straightforward and based on film theory, maintaining the desired simplicity. It replaces the heat and mass transfer boundary conditions at infinity with the same conditions moved inward to the so-called film radius, δ_T for energy and δ_M for species. The film radii are defined, in terms of the droplet Nusselt number, Nu_d, for heat transfer, and the droplet Sherwood number, Sh_d, for mass transfer, as follows [31]:

$$\frac{\delta_T}{r_s} = \frac{Nu_d}{Nu_d - 2} \tag{35a}$$

$$\frac{\delta_M}{r_s} = \frac{Sh_d}{Sh_d - 2}\,. \tag{35b}$$

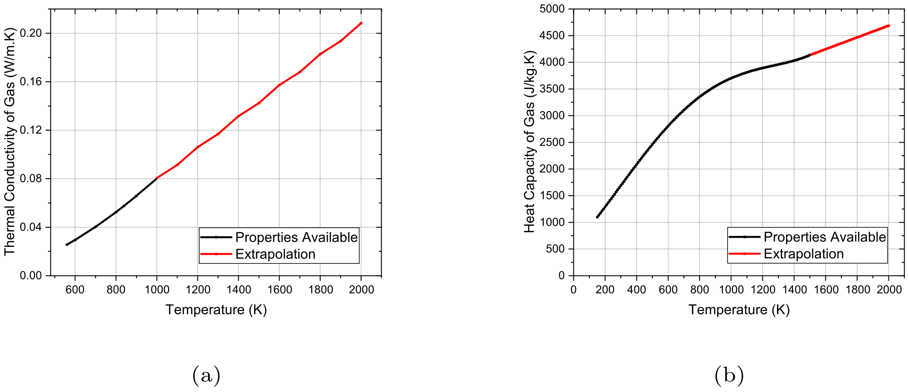

Fig. 25. Extrapolation of n-hexadecane (a) gas thermal conductivity, (b) gas heat capacity.
Source: Adapted from [73].

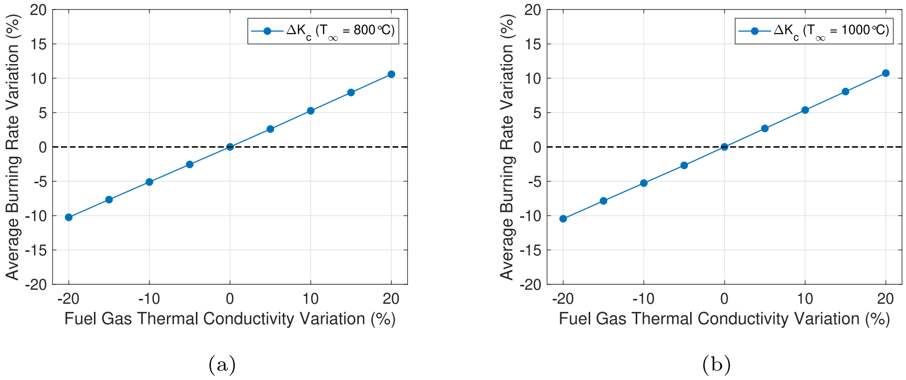

Fig. 26. Influence of the fuel gas thermal conductivity in the average droplet burning rate for: (a) $T_\infty = 800$ °C, (b) $T_\infty = 1000$ °C.

Note that $Nu_d = 2$ for a quiescent medium, and then one would recover $\delta_T \rightarrow \infty$. Since unity Lewis number is assumed, $Nu_d = Sh_d$. To evaluate Nu_d, Faeth [74] proposed the following correlation

$$Nu_d = 2 + \frac{0.555 Re_d^{1/2} Pr_g^{1/3}}{\left[1 + \frac{1.232}{Re_d Pr_g^{4/3}}\right]^{1/2}} \tag{36}$$

where Pr_g is the gas Prandtl number. Eq. (36) applies to both droplet evaporation and combustion and is valid for low and high Re_d values up to $Re_d = 1800$ [75]. Re_d in Eq. (36) was evaluated according to Eq. (11). U_{rel} was calculated using Eq. (12), where U_d was determined from the results of the experiments conducted and U_∞ was approximated to

$$U_\infty = \frac{Q_{inj}}{A_{tube}} \frac{\rho_\infty\left(T_{inj}\right)}{\rho_\infty\left(T_\infty\right)} \tag{37}$$

where $Q_{inj} = 9.5 \cdot 10^{-5}$ m^3/s is the air flow rate injected into the DTF, A_{tube} is the cross-sectional area of the DTF quartz tube, $A_{tube} = 3.42 \cdot 10^{-3}$ m^2, ρ_∞ is the air density and T_{inj} is the air injection temperature, estimated to be approximately 20 °C. ν_g in Eq. (11) and Pr_g in Eq. (36) were approximated to those of air and evaluated at a mean temperature $\overline{T}_2 = \left(T_f + T_\infty\right)/2$ [48]. Consequently, as previously stated by [31], the burning rate constant considering the convection effects can be defined as

$$K_c = \frac{4 k_g Nu_d}{\rho_l c_{pg}} \ln\left(1 + B_{o,q}\right). \tag{38}$$

Appendix D. Sensitivity analysis

In this section, the results obtained from the sensitivity analysis is presented for fuel gas thermal conductivity, heat capacity and absorptivity.

D.1. Fuel gas thermal conductivity

See Fig. 26.

D.2. Fuel gas heat capacity

See Fig. 27.

D.3. Absorptivity

See Fig. 28.

Appendix E. Radiation absorption

To understand the effective relevance of radiation absorption in a nanofuel droplet, an analysis of the different energy transfer mechanisms was performed. These results were acquired disregarding the particle agglomeration influence to highlight the radiation absorption effect. Figs. 29 and 30 show that by increasing the furnace temperature, the role of the radiation becomes more pronounced.

In addition, increasing the particle concentration slightly increase the radiation absorption by the nanoparticles (see Fig. 31).

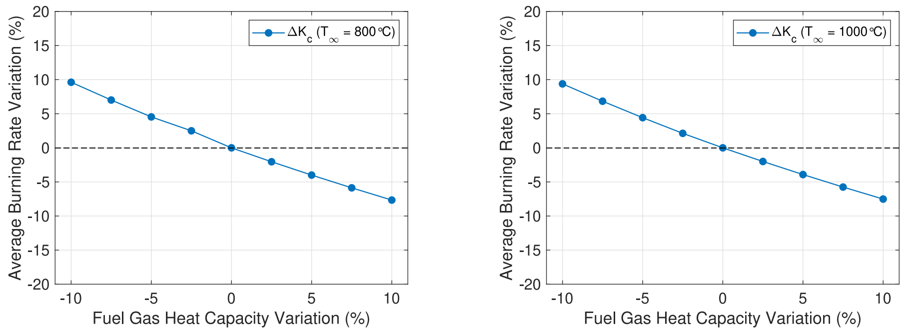

(a)

(b)

Fig. 27. Influence of the fuel gas heat capacity in the average droplet burning rate for: (a) $T_\infty = 800$ °C, (b) $T_\infty = 1000$ °C.

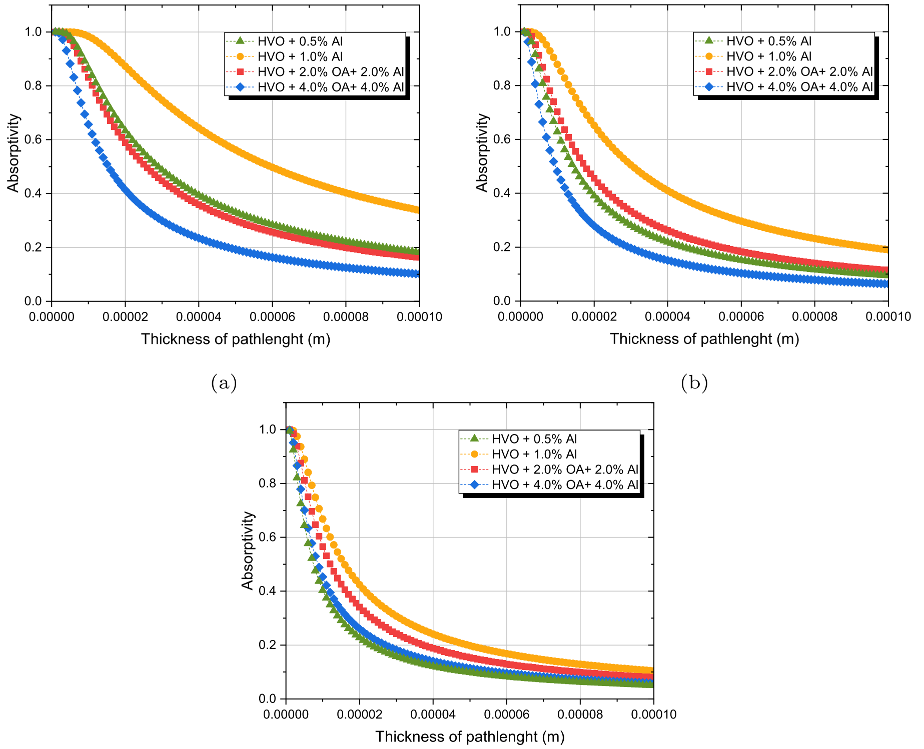

(a)

(b)

(c)

Fig. 28. Absorptivity as a function of the pathlength thickness for (a) $\lambda = 2.7$ μm (a) $\lambda = 4.3$ μm and (c) $\lambda = 7.0$ μm.

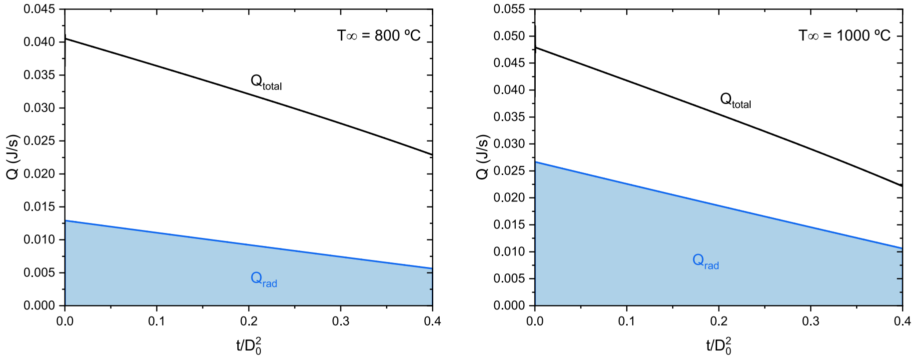

(a)

(b)

Fig. 29. Modeling results for the energy transfer mechanisms considering a particle concentration of 1% for both furnace temperatures (a) $T_\infty = 800$ °C, (b) $T_\infty = 1000$ °C.

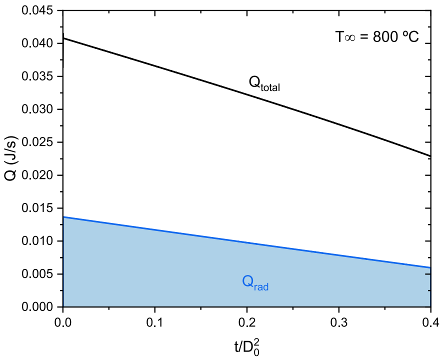

(a) (b)

Fig. 30. Modeling results for the energy transfer mechanisms considering a particle concentration of 4% for both furnace temperatures (a) $T_\infty = 800$ °C, (b) $T_\infty = 1000$ °C.

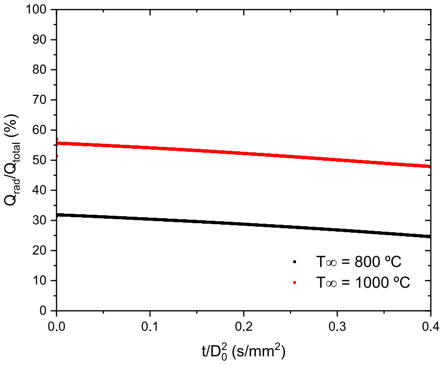

(a) (b)

Fig. 31. Relation between Q_{rad} and Q_{total} at a particle concentration of (a) 1% and (b) 4% for both furnace temperatures $T_\infty = 800$ °C, (b) $T_\infty = 1000$ °C.

References

[1] Ritchie H, Roser M. Our world in data: CO2 and greenhouse gas emissions. 2019.
[2] Cabrera E, de Sousa JMM. Use of sustainable fuels in aviation—A review. Energies 2022;15(7):2440.
[3] Dahal K, Brynolf S, Xisto C, Hansson J, Grahn M, Grönstedt T, Lehtveer M. Techno-economic review of alternative fuels and propulsion systems for the aviation sector. Renew Sustain Energy Rev 2021;151:111564.
[4] Ferrão IA, Silva AR, Moita AS, Mendes MA, Costa MM. Combustion characteristics of a single droplet of hydroprocessed vegetable oil blended with aluminum nanoparticles in a drop tube furnace. Fuel 2021;302:121160.
[5] Lee CC, Tran M-V, Tan BT, Scribano G, Chong CT. A comprehensive review on the effects of additives on fundamental combustion characteristics and pollutant formation of biodiesel and ethanol. Fuel 2021;288:119749.
[6] Basu S, Miglani A. Combustion and heat transfer characteristics of nanofluid fuel droplets: A short review. Int J Heat Mass Transfer 2016;96:482–503.
[7] Emekwuru NG. Nanofuel droplet evaporation processes. J Indian Inst Sci 2019;99(1):43–58.
[8] Gan Y, Qiao L. Evaporation characteristics of fuel droplets with the addition of nanoparticles under natural and forced convections. Int J Heat Mass Transfer 2011;54(23–24):4913–22.
[9] Zhu B, Sun Y, Guo P, Liu J, et al. Nano-sized copper oxide enhancing the combustion of aluminum/kerosene-based nanofluid fuel droplets. Combust Flame 2022;240:112028.
[10] Wang R, Pan G, Qian S, Li L, Zhu Z. Influence of nanoparticles on the evaporation behavior of nanofluid droplets: A Dh law and underlying mechanism. Langmuir 2019;36(4):919–30.
[11] Javed I, Baek SW, Waheed K. Effects of dense concentrations of aluminum nanoparticles on the evaporation behavior of kerosene droplet at elevated temperatures: The phenomenon of microexplosion. Exp Therm Fluid Sci 2014;56:33–44.
[12] Gan Y, Qiao L. Combustion characteristics of fuel droplets with addition of nano and micron-sized aluminum particles. Combust Flame 2011;158(2):354–68.
[13] Ghamari M, Ratner A. Combustion characteristics of colloidal droplets of jet fuel and carbon based nanoparticles. Fuel 2017;188:182–9.
[14] Ferrão IA, Mendes MA, Moita AS, Silva AR. The addition of particles to an alternative jet fuel. Fuels 2022;3(2):184–206.
[15] Yadav AK, Nandakumar K, Srivastava A, Chowdhury A. Combustion of rocket-grade kerosene droplets loaded with graphene nanoplatelets—A search for reasons behind optimum mass loadings. Combust Flame 2019;203:1–13.
[16] Liu JZ, Chen BH, Wu TT, Yang WJ, Zhou JH. Ignition and combustion characteristics and agglomerate evolution mechanism of aluminum in nAl/JP-10 nanofluid fuel. J Therm Anal Calorim 2019;137:1369–79.
[17] Mosadegh S, Ghaffarkhah A, van der Kuur C, Arjmand M, Kheirkhah S. Graphene oxide doped ethanol droplet combustion: Ignition delay and contribution of atomization to burning rate. Combust Flame 2022;238:111748.
[18] Tanvir S, Qiao L. Droplet burning rate enhancement of ethanol with the addition of graphite nanoparticles: Influence of radiation absorption. Combust Flame 2016;166:34–44.
[19] Tyagi H, Phelan PE, Prasher R, Peck R, Lee T, Pacheco JR, Arentzen P. Increased hot-plate ignition probability for nanoparticle-laden diesel fuel. Nano Lett 2008;8(5):1410–6.
[20] Javed I, Baek SW, Waheed K. Autoignition and combustion characteristics of heptane droplets with the addition of aluminium nanoparticles at elevated temperatures. Combust Flame 2015;162(1):191–206.
[21] Javed I, Baek SW, Waheed K. Autoignition and combustion characteristics of kerosene droplets with dilute concentrations of aluminum nanoparticles at elevated temperatures. Combust Flame 2015;162(3):774–87.
[22] Kim DM, Baek SW, Yoon J. Ignition characteristics of kerosene droplets with the addition of aluminum nanoparticles at elevated temperature and pressure. Combust Flame 2016;173:106–13.
[23] Gan Y, Qiao L. Radiation-enhanced evaporation of ethanol fuel containing suspended metal nanoparticles. Int J Heat Mass Transfer 2012;55(21–22):5777–82.
[24] Tanvir S, Qiao L. Effect of addition of energetic nanoparticles on droplet-burning rate of liquid fuels. J Propuls Power 2015;31(1):408–15.
[25] Gerken WJ, Thomas AV, Koratkar N, Oehlschlaeger MA. Nanofluid pendant droplet evaporation: Experiments and modeling. Int J Heat Mass Transfer 2014;74:263–8.
[26] Wei Y, Deng W, Chen R-H. Effects of insoluble nano-particles on nanofluid droplet evaporation. Int J Heat Mass Transfer 2016;97:725–34.
[27] Tanvir S, Biswas S, Qiao L. Evaporation characteristics of ethanol droplets containing graphite nanoparticles under infrared radiation. Int J Heat Mass Transfer 2017;114:541–9.

[28] Li S, Yang Q, Ye L, Du H, Zhang Z, Huang X, Xu J. Effect of nanoparticle concentration on physical and heat-transfer properties and evaporation characteristics of graphite/n-decane nanofluid fuels. ACS Omega 2022;7(4):3284–92.

[29] Godsave G. Studies of the combustion of drops in a fuel spray—the burning of single drops of fuel. In: Symposium (international) on combustion. Vol. 4, Elsevier; 1953, p. 818–30.

[30] Spalding DB. Combustion of liquid fuels. Nature 1950;165(4187):160.

[31] Turns SR, et al. Introduction to combustion, vol. 287, McGraw-Hill Companies New York, NY, USA; 1996.

[32] Law CK. Recent advances in droplet vaporization and combustion. Prog Energy Combust Sci 1982;8(3):171–201. http://dx.doi.org/10.1016/0360-1285(82)90011-9.

[33] Irfan M, Muradoglu M. A front tracking method for particle-resolved simulation of evaporation and combustion of a fuel droplet. Comput & Fluids 2018;174:283–99.

[34] Abramzon B, Sirignano WA. Droplet vaporization model for spray combustion calculations. Int J Heat Mass Transfer 1989;32(9):1605–18.

[35] Downingm CG. The evaporation of drops of pure liquids at elevated temperatures: Rates of evaporation and wet-bulb temperatures. AIChE J 1966;12(4):760–6.

[36] Wong S-C, Lin A-C. Internal temperature distributions of droplets vaporizing in high-temperature convective flows. J Fluid Mech 1992;237:671–87.

[37] Awasthi I, Pope DN, Gogos G. Effects of the ambient temperature and initial diameter in droplet combustion. Combust Flame 2014;161(7):1883–99.

[38] Awasthi I, Gogos G, Sundararajan T. Effects of size on combustion of isolated methanol droplets. Combust Flame 2013;160(9):1789–802.

[39] Gan Y, Qiao L. Optical properties and radiation-enhanced evaporation of nanofluid fuels containing carbon-based nanostructures. Energy Fuels 2012;26(7):4224–30.

[40] Starik A, Savel'ev A, Titova N. Specific features of ignition and combustion of composite fuels containing aluminum nanoparticles. Combust Explos Shock Waves 2015;51:197–222.

[41] Wu B, Wu F, Wang P, He A, Wu H. Ignition and combustion of hydrocarbon fuels enhanced by Aluminum Nanoparticle Additives: Insights from reactive molecular dynamics simulations. J Phys Chem C 2021;125(21):11359–68.

[42] Corporation N. Neste renewable diesel handbook. Technical report, 2020.

[43] Javed I, Baek SW, Waheed K, Ali G, Cho SO. Evaporation characteristics of kerosene droplets with dilute concentrations of ligand-protected aluminum nanoparticles at elevated temperatures. Combust Flame 2013;160(12):2955–63.

[44] Han W, Dai B, Liu J, Sun Y, Zhu B, Liu X. Ignition and combustion characteristics of heptane-based nanofluid fuel droplets. Energy Fuels 2019;33(10):10282–9.

[45] Yang Q, Li S, Ye L, Huang X. Understanding of contradiction on concentration effect on stability, physical properties, evaporation and microexplosion characteristics of Al/JP-10/Oleic Acid Nanofluid Fuel. Nanomaterials 2022;12(19):3446.

[46] Giedt RJ, Koch PD, Weissleder R. Single cell analysis of drug distribution by intravital imaging. PLoS One 2013;8(4):e60988.

[47] Gong Y, Kaario O, Tilli A, Larmi M, Tanner F. A computational investigation of hydrotreated vegetable oil sprays using RANS and a modified version of the RNG k-ε model in OpenFOAM. Tech. rep., SAE Technical Paper; 2010.

[48] Law CK, Williams FA. Kinetics and convection in the combustion of alkane droplets. Combust Flame 1972;19(3):393–405. http://dx.doi.org/10.1016/0010-2180(72)90009-0.

[49] Law C. Recent advances in droplet vaporization and combustion. Prog Energy Combust Sci 1982;8(3):171–201.

[50] Bergman TL, Lavine AS, Incropera FP, DeWitt DP. Introduction to heat transfer. John Wiley & Sons; 2011.

[51] Megias-Alguacil D, Gauckler LJ. Capillary and van der Waals forces between uncharged colloidal particles linked by a liquid bridge. Colloid Polym Sci 2010;288:133–9.

[52] Tanvir S, Qiao L. Effect of addition of energetic nanoparticles on droplet-burning rate of liquid fuels. J Propuls Power 2015;31(1):408–15. http://dx.doi.org/10.2514/1.B35500.

[53] Bergman TL, Incropera FP, DeWitt DP, Lavine AS. Fundamentals of heat and mass transfer. John Wiley & Sons; 2011.

[54] Marchese AJ, Dryer FL. The effect of non-luminous thermal radiation in microgravity droplet combustion. Combust Sci Technol 1997;124(1–6):371–402.

[55] Hazra S, Ghosh S, Nandi T. Photo-thermal conversion characteristics of carbon black-ethylene glycol nanofluids for applications in direct absorption solar collectors. Appl Therm Eng 2019;163:114402.

[56] Khullar V, Tyagi H, Hordy N, Otanicar TP, Hewakuruppu Y, Modi P, Taylor RA. Harvesting solar thermal energy through nanofluid-based volumetric absorption systems. Int J Heat Mass Transfer 2014;77:377–84.

[57] Wei Y, Deng W, Chen R-H. Effects of insoluble nano-particles on nanofluid droplet evaporation. Int J Heat Mass Transfer 2016;97:725–34. http://dx.doi.org/10.1016/j.ijheatmasstransfer.2016.02.052.

[58] Bennewitz JW, Badakhshan A, Talley DG. Combustion characteristics of suspended hydrocarbon fuel droplets with various nanoenergetic additives. Combust Sci Technol 2021;193(12):2111–36.

[59] Boel E, Koekoekx R, Dedroog S, Babkin I, Vetrano MR, Clasen C, Van den Mooter G. Unraveling particle formation: From single droplet drying to spray drying and electrospraying. Pharmaceutics 2020;12(7).

[60] de Souza Lima R, Ré M-I, Arlabosse P. Drying droplet as a template for solid formation: A review. Powder Technol 2020;359:161–71. http://dx.doi.org/10.1016/j.powtec.2019.09.052.

[61] Mezhericher M, Levy A, Borde I. Modelling the morphological evolution of nanosuspension droplet in constant-rate drying stage. Chem Eng Sci 2011;66(5):884–96. http://dx.doi.org/10.1016/j.ces.2010.11.028.

[62] Maurice U, Mezhericher M, Levy A, Borde I. Drying of droplet containing insoluble nanoscale particles: Numerical simulations and parametric study. Drying Technol 2013;31(15):1790–807. http://dx.doi.org/10.1080/07373937.2013.823443.

[63] Gerken WJ, Thomas AV, Koratkar N, Oehlschlaeger MA. Nanofluid pendant droplet evaporation: Experiments and modeling. Int J Heat Mass Transfer 2014;74:263–8. http://dx.doi.org/10.1016/j.ijheatmasstransfer.2014.03.031.

[64] Li H, Rosebrock CD, Wu Y, Wriedt T, Mädler L. Single droplet combustion of precursor/solvent solutions for nanoparticle production: Optical diagnostics on single isolated burning droplets with micro-explosions. Proc Combust Inst 2019;37(1):1203–11. http://dx.doi.org/10.1016/j.proci.2018.06.133.

[65] Gan Y, Lim YS, Qiao L. Combustion of nanofluid fuels with the addition of boron and iron particles at dilute and dense concentrations. Combust Flame 2012;159(4):1732–40. http://dx.doi.org/10.1016/j.combustflame.2011.12.008.

[66] Rumpf H. Particle technology. 1st ed.. Chapman and Hall; 1990.

[67] Li H, Rosebrock CD, Wu Y, Wriedt T, Mädler L. Single droplet combustion of precursor/solvent solutions for nanoparticle production: Optical diagnostics on single isolated burning droplets with micro-explosions. Proc Combust Inst 2019;37(1):1203–11.

[68] Ferrão I, Mendes M, Moita A, Silva AR. Experimental investigation of disruptive burning phenomena on nanofuel droplets. In: 20th international symposium on applications of laser and imaging techniques to fluid mechanics. Center for Innovation, Technology and Policy Research IN+.

[69] Pandey K, Basu S, Gautham V, Potnis A, Chattopadhyay K. Self-tuning and topological transitions in a free-falling nanofuel droplet flame. Combust Flame 2020;220:144–56.

[70] Barth A. Infrared spectroscopy of proteins. Biochim Biophys Acta (BBA)-Bioenerg 2007;1767(9):1073–101.

[71] Hinkov B, Pilat F, Lux L, Souza PL, David M, Schwaighofer A, Ristanić D, Schwarz B, Detz H, Andrews AM, et al. A mid-infrared lab-on-a-chip for dynamic reaction monitoring. Nat Commun 2022;13(1):4753.

[72] Kafle B, Böcker U, Wubshet SG, Dankel K, Måge I, Marion O, Afseth NK. Fourier-transform infrared spectroscopy for characterization of liquid protein solutions: A comparison of two sampling techniques. Vib Spectrosc 2023;124:103490.

[73] Yaws CL. Chemical properties handbook. McGraw-Hill Education; 1999.

[74] Faeth GM. Current status of droplet and liquid combustion. Prog Energy Combust Sci 1977;3(4):191–224. http://dx.doi.org/10.1016/0360-1285(77)90012-0.

[75] Law CK. Combustion physics. Cambridge University Press; 2006.